

# Exploring the stellar streams and satellites around the giant low surface brightness galaxy Malin 1

Roy O. E. Bustos-Espinoza<sup>1,2</sup>, Matias Blaña<sup>3</sup>, Gaspar Galaz<sup>1</sup>, Marcelo D. Mora<sup>4</sup>, Junais<sup>5,6</sup>, Mousumi Das<sup>7</sup>,  
Sudhanshu Barway<sup>7</sup>, Ankit Kumar<sup>8</sup>, Evelyn J. Johnston<sup>9</sup>, and Thomas Puzia<sup>1</sup>

<sup>1</sup> Instituto de Astrofísica, Pontificia Universidad Católica de Chile, Vicuña Mackenna 4860, Macul, Santiago, Chile  
e-mail: robustos@uc.cl

<sup>2</sup> Instituto de Investigaciones Físicas, Universidad Mayor de San Andrés, La Paz, Estado Plurinacional de Bolivia

<sup>3</sup> Centro Espacial Nacional, Fuerza Aérea de Chile, Av. Pedro Aguirre Cerda 5500, Cerrillos, Santiago, Chile.

<sup>4</sup> Las Campanas Observatory, Carnegie Observatories, Casilla 601, La Serena, 7820436, Chile

<sup>5</sup> Instituto de Astrofísica de Canarias, Vía Láctea S/N, E-38205 La Laguna, Spain

<sup>6</sup> Departamento de Astrofísica, Universidad de La Laguna, E-38206 La Laguna, Spain

<sup>7</sup> Indian Institute of Astrophysics, Koramangala, Bangalore 560034, India

<sup>8</sup> Instituto de Astrofísica, Departamento de Física y Astronomía, Facultad de Ciencias Exactas, Universidad Andres Bello, Fernandez Concha 700, Las Condes, Santiago RM, Chile

<sup>9</sup> Instituto de Estudios Astrofísicos, Facultad de Ingeniería y Ciencias, Universidad Diego Portales, Av. Ejército Libertador 441, Santiago, Chile

Received May 15, 2026; accepted May 15, 2026

## ABSTRACT

*Context.* Giant Low Surface Brightness galaxies (gLSBGs), such as Malin 1, host extended stellar and gaseous discs exceeding 100 kpc in radius. Their formation and evolution remain debated, with interactions with satellite galaxies and accretion streams proposed as key contributors. Malin 1 presents multiple nearby and distant satellites. Additionally, it exhibits two giant stellar streams, the largest extending 200 kpc in projection, likely related to past interactions.

*Aims.* We investigate the orbital dynamics of Malin 1's satellites and their possible connections with the observed stellar streams, testing their nature with different formation scenarios.

*Methods.* We constructed gravitational potentials for Malin 1 using optical and HI rotation curve data, incorporating stellar, gaseous, and dark matter (DM) components. We explored a wide orbital parameter space to determine whether the candidate progenitors of the stellar streams could have originated from past interactions, testing both Navarro-Frenk-White (NFW) and the pseudo-isothermal (ISO) halo profiles.

*Results.* Among several explored scenarios, some produced bound orbital solutions. The ISO halo model, with mass of  $M_{\text{virial}} \approx 2.6 \times 10^{12} M_{\odot}$ , favours bound satellite orbits more than the NFW model, that has a lower mass of  $M_{\text{virial}} \approx 1.4 \times 10^{12} M_{\odot}$ . These orbital models show that the giant stellar streams could be substructures of some satellites galaxies located along their leading and trailing orbital trajectories. Furthermore, our analysis indicates that the most distant Malin 1 satellite (eM1) could have reached its orbital pericenter  $\sim 1.6$  Gyr ago, while the nearest companions could have interacted as early as  $\sim 100$  Myr ago. At the same time, one of the closest companions would still be under a strong interaction. Another close companion displays both leading and trailing arms in a radial orbit although show us a polar orbit also. Furthermore, we identify some unbound orbital solutions that could link some satellites with streams.

*Conclusions.* The observed alignment of satellites and streams indicates that past interactions likely shaped aspects of Malin 1's morphology. Our orbital modelling constrains possible progenitors of the observed stellar streams and their orbital histories, providing new insights into the dynamical evolution of gLSBGs. Our findings are consistent with results reported very recently by other studies using Malin 1 kinematic data.

**Key words.** Extragalactic astronomy – Galaxies: evolution – Galaxies: interactions – Galaxies: kinematics and dynamics – Gravitation – Galaxies: spiral

## 1. Introduction

Disney (1976) suggested the possibility that there are galaxies with a surface brightness (SB) lower than the empirical limit proposed by Freeman (1970), which defined the characteristic central surface brightness of disc galaxies around  $21.65 B \text{ mag arcsec}^{-2}$ . This threshold was based on observations of high-surface-brightness spirals and was initially thought to represent a universal feature of disc galaxies. Since then, the discovery rate of low surface brightness Galaxies (LSBGs) has been boosted by advances in observational techniques and deeper sky surveys,

leading to a growing recognition of their importance in galaxy formation and evolution (Du et al. 2020).

In general terms, LSBGs exhibit a central surface brightness fainter than  $23.5 B \text{ mag arcsec}^{-2}$  (Impey & Bothun 1997). These galaxies display poor star formation rates, low metallicity, and extended HI gas discs; characteristics shared with giant low surface brightness galaxies (gLSBGs), which appear as massive systems typically existing in isolation and having sizes larger than that of the Milky Way (MW) up to the 25th isophote (Das 2013).

Malin 1, one of the most iconic gLSBGs due to its immense size and faintness, was discovered serendipitously by [Bothun et al. \(1987\)](#). This particular gLSBG has a bar structure and shows a LINER nucleus ([Barth 2007](#)). The evidence indicates that the bar resulted from several star formation events, along with the discovery of compact sources, pointing to a possible double nucleus system ([Johnston et al. 2024](#)). [Ogle et al. \(2016, 2019\)](#) report the discovery of a large sample of the most optically luminous, largest, and most massive spiral galaxies in the universe, called super spirals, which could be analogous to Malin 1; however, Malin 1 is still the largest stellar disc known ([Ogle et al. 2016, 2019](#)), but it has a much lower star formation rate  $\sim 1.2M_{\odot}\text{yr}^{-1}$  ([Lelli et al. 2010](#); [Junais et al. 2024](#)).

Malin 1 also presents HII regions, a radial decrease in the surface density of the star formation rate, reduced metal content, and flattening in the outer disc ([Junais et al. 2024](#)). These characteristics provide clues about the development of the disc, with the most likely scenario involving the accretion of pre-enriched gas from a previous merger ([Junais et al. 2024](#); [Zhu et al. 2018](#)). Furthermore, the galaxy is characterized by a low dust content and a minimal presence of molecular gas ([Gerritsen & De Blok 1999](#); [Galaz et al. 2022](#); [Junais et al. 2024](#); [Galaz et al. 2024](#)).

Moreover, an optical map reveals a cavity in the southern part, between the arms ([Galaz et al. 2015](#)). This cavity could be due to feedback from star formation, as the HI map shows a nearby asymmetric substructure ([Lelli et al. 2010](#)), or the action of supernova-driven winds expelling gas, similar to phenomena observed in other galaxies such as the Hoag galaxy ([Bannikova 2018](#)), the Fireworks galaxy ([Blair et al. 2019](#)), NGC 1300 ([Maeda et al. 2022](#)), or the gLSBG UGC 1382 ([Saburova et al. 2022](#)). A northern warp in the HI disc shows axis asymmetry, possibly due to the accretion of a paired system of two gas-rich satellite galaxies. This can be evidence of ongoing interaction ([Saha et al. 2021](#)).

Studies reveal that Malin 1 interacts with at least two companion galaxies, identified as Malin 1B and the SDSS J123708.91+142253.2 ([Reshetnikov et al. 2010](#); [Galaz et al. 2015](#)). The latter is also referred to as exo-Malin 1, a designation initially introduced by [Bustos Espinoza et al. \(2024b,a\)](#), or eM1 for brevity; both are associated satellite galaxies. In addition, Malin 1A is part of the Malin 1 system and, together with Malin 1B, is classified as a compact elliptical (cE) ([Saburova et al. 2022](#)). A recent study by [Junais et al. \(2024\)](#) identified several H $\alpha$  regions, including Malin 1C, which is part of the Malin 1 galaxy and may be an ultra-diffuse galaxy (UDG) that interacts with the core galaxy ([Ji et al. 2021](#)). Malin 1C has possibly been stripped of gas and outlying stars by tidal interactions ([Kazantzidis et al. 2004](#)). Malin 1B and exo-Malin 1 are situated at distances of 14 kpc and 350 kpc, toward the south-east and north-west, respectively ([Reshetnikov et al. 2010](#)). These objects, along with others, are clearly illustrated in detail in Fig. 1.

According to [Saha et al. \(2021\)](#), exo-Malin 1 may play a role in star formation within the central bar, while the accretion of Malin 1B could bolster star formation in the arms and bulge ([Saha et al. 2021](#)). As noted by [Saburova et al. \(2023\)](#) and [Peñarrubia et al. \(2006\)](#), extended discs in gLSBGs could develop through minor mergers involving gas-rich satellites, possibly applicable to exo-Malin 1, Malin 1B, Malin 1A, and Malin 1C.

Tidal stellar streams exemplify the continuous merging and accretion of galaxies, a key process in the formation of structures within the Universe ([Niederste-Ostholt et al. 2012](#)). Several well-studied examples illustrate the remnants of disrupted

dwarf galaxies and their tidal debris. The Sagittarius stream, which originates in the dwarf galaxy of Sagittarius, demonstrates that progenitors can lie several to tens of degrees away from their associated streams ([Niederste-Ostholt et al. 2012](#); [Bonaca et al. 2021](#)). Similarly, a vast stellar stream extending more than 500 kpc has been identified on the outskirts of the Coma cluster, likely formed from the destruction of a dwarf galaxy and providing key insights into the gravitational potential of the cluster ([Román et al. 2023](#)). The spatial relationship between a satellite and its debris depends on its orbital phase: near the apocenter, the material tends to accumulate into overdensities, while near the pericenter, the tidal stream stretches along the orbit and compresses perpendicular to its motion due to its acceleration and host tidal field (e.g. [Niederste-Ostholt et al. 2012](#); [Smith et al. 2013](#); [Blaña et al. 2015](#)).

Analysis of the luminosity of the stream progenitors suggests that they were absorbed during relatively early formation periods ([Vera-Casanova et al. 2022](#)). Moreover, recent studies of the giant spiral galaxy Malin 2 revealed faint tidal structures surrounding the main host ([Junais et al. 2025](#)), suggesting that tidal interactions and mergers may be common processes in ultra-low surface brightness systems.

Various hypotheses are developed here regarding the origin of gLSBG. According to [Noguchi \(2001\)](#), gLSBGs evolve from standard spiral galaxies through dynamic changes over time. Their formation is influenced by environmental factors, including large galaxies in voids that feature conventional bulges coupled with extensive LSB discs ([Hoffman et al. 1992](#)). Within the hierarchical formation paradigm, mergers between a central galaxy and its satellite companions may explain the considerable size observed ([Peñarrubia et al. 2006](#)). Although the origins and properties remain partially unknown, some cosmological simulations point to these alignment-driven mergers as the key to such large-scale development ([Zhu et al. 2023](#)). Moreover, [Zhu et al. \(2018\)](#) identified that a significant fraction of the cold gas at redshift zero originated from the cooling of the hot halo gas, a process triggered by the merger of a pair of interacting galaxies.

The  $\Lambda$ -Cold Dark Matter ( $\Lambda$ CDM) cosmology theory suggests that the disruption of satellite galaxies is a frequent process in the lifetime of massive galaxies ([Martínez-Delgado et al. 2023](#); [Miro-Carretero et al. 2024](#)). The extended size of the disc might result from the impact of two or more galaxies merging. This formation mechanism aligns with the existing theories of formation of gLSBGs ([Zhu et al. 2018](#)). As [Román et al. \(2023\)](#) pointed out, such giant, faint stellar streams may exist in galaxy clusters and groups according to  $\Lambda$ -CDM. So, the presence of streams in the Malin 1 system could be evidence that not all gLSBGs are isolated, in contrast to [Das \(2013\)](#), who argued that gLSBGs are usually isolated, often near the edges of voids, and that their lack of interactions contributes to their slow evolution. Research involving cosmological simulations ([Zhu et al. 2018](#)) illustrates that smaller galaxies, often termed intruders, can interact with larger galaxies, leading to the formation of a gLSBG that shares notable similarities with Malin 1. Similarly, [Mapelli et al. \(2008\)](#) proposed that stimulated accretion might explain the exceptionally large disc size of Malin 1. Additionally, [Zhu et al. \(2018\)](#) indicated that a collision involving three galaxies could produce a gas-rich, giant low-surface-brightness galaxy.

This paper investigates Malin 1 and its surroundings. We analyze possible orbital configurations of its satellite galaxies, including both leading and trailing segments, to comprehend their impact on its structure, kinematics, and evolutionary progression.

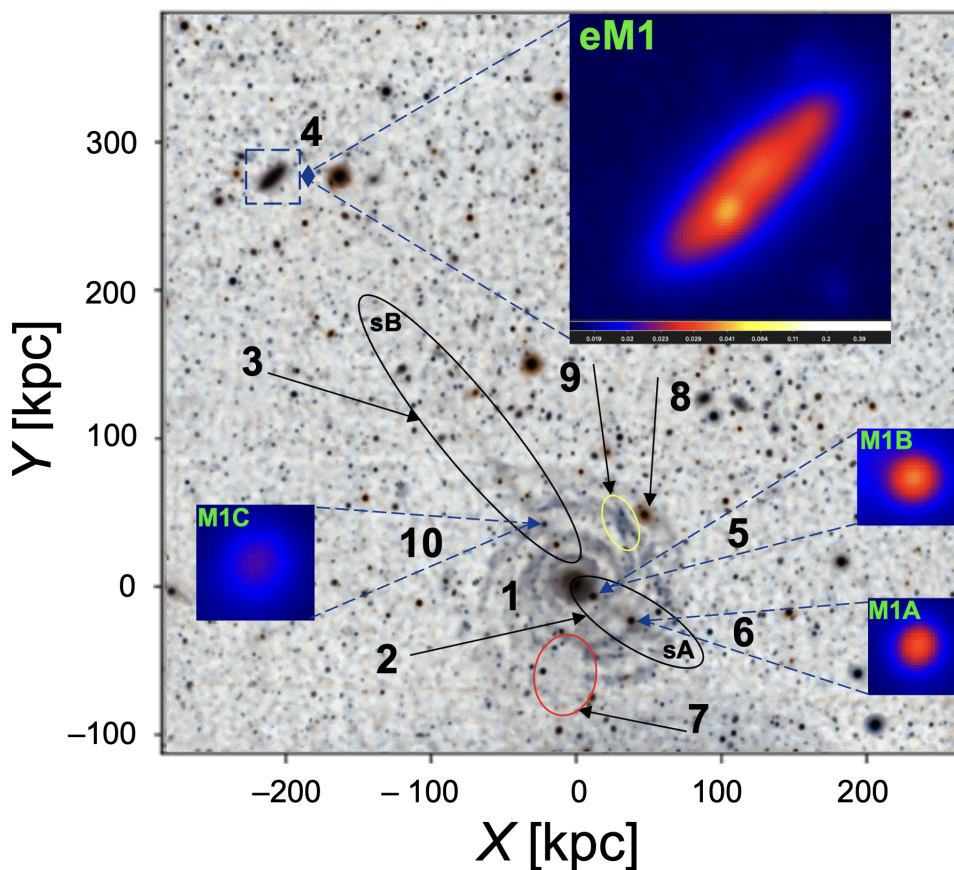


Fig. 1: Optical view in  $g$ , and  $r$  band, of Malin 1 and their environment using Magellan/Clay telescope (Galaz et al. 2015). The figure equatorial coordinates are converted into  $X$ ,  $Y$  in kpc units, adopting an angular scale of  $1.557$  kpc per  $\text{arcsec}^{-1}$ , with the origin centred at the core of Malin 1. The intensity color scale is consistent throughout all sub-panels, with its arbitrary units defined by the scale shown in the large sub-panel (4). Labels include: **1.** Optical view,  $g$ , and  $r$  band, of Malin 1 displaying Galaz et al. (2015). **2.** Proposed stream A (sA), possible linking Malin 1A, Malin 1B, and Malin 1. **3.** Proposed stream B (sB), aligned in projection with exo-Malin 1, Malin 1C, and Malin 1. **4.** The satellite galaxy SDSS J123708.91+142253.2 (Reshetnikov et al. 2010), referred here as exo-Malin 1 (eM1), located at coordinates  $X = -211.38$  kpc,  $Y = 277.78$  kpc. The separation between eM1 and Malin 1 is  $\sim 350$  kpc (Reshetnikov et al. 2010; Galaz et al. 2015). There is a clear offset between the central brightness peak and the geometrical centre (zoom-in), which could be a result of past interactions. **5.** Malin 1B (M1B), a compact elliptical (cE) interacting galaxy (Saburova et al. 2022). **6.** Malin 1A, interacting cE galaxy examined in Saburova et al. (2022). **7.** Cavity, observed a low stellar density region displaying an apparent gap between spiral arms (red ellipse). **8.** A distant background galaxy ( $z=0.3639$ ). **9.** Yellow ellipse indicating clumps within the spiral arms; their structure suggests regions of star formation or clusters of newly formed stars, based on VLT-MUSE observations (Junais et al. 2024). **10.** An Ultra Diffuse Galaxy (UDG) candidate (Ji et al. 2021), with VLT-MUSE data (Junais et al. 2024) showing a young star formation region with redshift  $z = 0.08292$ . It is situated at  $\sim 46.75$  kpc from Malin 1 centre, and is referred here as Malin 1C (M1C).

The structure of this article is as follows. Section 2 describes the observed substructures. Section 3 details the modelling approach for the Malin 1 system. Section 3.1 provides the observational data and associated constraints. Section 3.2 discusses the gravitational potential of Malin 1, and Section 3.3 outlines scenarios to explore progenitor candidates of the stellar streams, including initial setups. Section 4 evaluates the results, and Section 5 discusses and interprets our findings. The conclusion is found in Section 6. Furthermore, two appendices summarize the optimal parameters and describe how prior knowledge is integrated into our model.

For our calculations, we used a flat  $\Lambda$ CDM cosmology with  $H_0$  set at  $70$   $\text{km s}^{-1} \text{Mpc}^{-1}$ ,  $\Omega_M = 0.27$ , and  $\Omega_\Lambda = 0.73$ . This results in a projected plate scale of  $1.557$  kpc  $\text{arcsec}^{-1}$  and a luminosity distance to Malin 1 of  $377$  Mpc.

## 2. Observed substructures in the Malin 1 system

This section presents a summary of the features identified in the optical image of Malin 1 (Galaz et al. 2015). The environment of Malin 1, observed in the  $g$  and  $r$  bands with the  $6.5$  m *Magellan/Clay* telescope, is shown in Fig. 1, and the listed substructures are indicated by arrows that follow the same numbering. The essential characteristics are listed in Table 1. Among the relevant properties of the Malin 1 system, the following are noteworthy:

- 1 Malin 1: the giant low surface brightness galaxy comprises a dual structure: a central bulge-bar and HSB disc resembling a Sa/SB galaxy with a radius under  $10$  kpc, and an extended, gas-rich outer LSB region with an optical diameter of  $240$  kpc (Barth 2007; Moore & Parker 2006). This last component features the most extensive known stellar disc, reaching a surface brightness of approximately  $28.0$   $B$

Table 1: Properties of the Malin 1 galaxy. Morphology, luminosity distance ( $D_L$ ), V-band absolute magnitude ( $M_V$ ), central surface brightness in the B ( $\mu_{0,B}$ ) and V band ( $\mu_{0,V}$ ), respectively, HI gas mass range ( $M_{\text{HI}}$ ), active galactic nucleus (AGN), right ascension ( $\alpha$ ), declination ( $\delta$ ), redshift ( $z$ ), galaxy’s Heliocentric systemic velocity ( $V_{\odot}^*$ ), optical diameter ( $D_{\text{opt}}$ ), inclination ( $i$ ), Luminosity r-band ( $L_r$ )

Property	
Morphology	SB0/a <sup>a</sup>
$D_L$	$377 \pm 8$ Mpc <sup>b</sup>
$M_V$	$-22.9 \pm 0.4$ mag <sup>c</sup>
$\mu_{0,B}$	$\sim 28.0$ mag arcsec <sup>-2</sup> <sup>d</sup>
$\mu_{0,V}$	$\sim 25.5$ mag arcsec <sup>-2</sup> <sup>e</sup>
$M_{\text{HI}}$	$4 - 7 \times 10^{10} M_{\odot}$ <sup>f</sup>
AGN	LINER <sup>g</sup>
$\alpha$ (J2000)	$12^{\text{h}}36^{\text{m}}59.35^{\text{s}}$ <sup>h</sup>
$\delta$ (J2000)	$+14^{\circ}19'49.16''$ <sup>h</sup>
$z$	$0.0827002$ <sup>h</sup>
$V_{\odot}^*$	$24775 \pm 10$ km s <sup>-1</sup> <sup>h</sup>
$D_{\text{opt}} \approx D_{\text{HI}} \approx 8D_{\text{MW}}$	$\sim 220$ kpc <sup>i</sup>
$i$	$38^{\circ} \pm 3^{\circ}$ <sup>j</sup>

References: <sup>a</sup> Barred lenticular galaxy with faint spiral arm features (Lelli et al. 2010). <sup>b</sup> (Lelli et al. 2010). <sup>c</sup> (Pickering et al. 1997), <sup>d</sup> (Galaz et al. 2015), <sup>e</sup> (Impey & Bothun 1997), <sup>f</sup> Pickering et al. (1997); Lelli et al. (2010), <sup>g</sup> (Barth 2007), <sup>h</sup>  $\alpha$ ,  $\delta$ , indicating equatorial coordinates (J2000 is the standard epoch),  $z$ , and  $V_{\odot}^*$  (Reshetnikov et al. 2010), <sup>i</sup> Optical and HI diameter, scaled to the Milky Way (Moore & Parker 2006), <sup>j</sup> (Lelli et al. 2010).

mag arcsec<sup>-2</sup> (Galaz et al. 2015; Boissier et al. 2016). The galaxy also possesses a large HI gas reservoir with a mass  $4-7 \times 10^{10} M_{\odot}$  (Pickering et al. 1997; Lelli et al. 2010). It also has a high specific angular momentum (Di Teodoro et al. 2023; Boissier et al. 2016; Salinas & Galaz 2021), and an extended flat rotation curve (Lelli et al. 2010; Pickering et al. 1997), all of which suggest the presence of a vast dark matter (DM) halo (Mo 2010).

- 2 Stream A (sA): As noted by Galaz et al. (2015), a possible stellar stream that could be possibly associated with two galaxies: Malin 1B, positioned at  $\sim 14$  kpc from the centre of Malin 1 (marked as point 5), and more likely Malin 1A which sits in the middle of the stream at  $\sim 45$  kpc from Malin 1 centre (marked as point 6), both in the south-west direction.
- 3 Stream B (sB): The largest ellipse shown in Fig. 1 outlines a structure found in Galaz et al. (2015) with an elongation that suggests a stellar stream, a jet, or a diffuse region (Boissier et al. 2016). Here, we call this stellar stream candidate Stream B. sB is significantly extended, reaching up to 200 kpc from the centre of Malin 1 in the direction of the satellite exo-Malin 1. If this extended feature corresponds to a stellar stream, then it could have formed from material—either stellar or gaseous—tidally stripped from a satellite galaxy. Here, we explore progenitors that could have had past encounters with Malin 1, removing material from the satellite, producing the stream-like structure.
- 4 exo-Malin 1 (eM1): a galaxy with a total luminosity of  $9.47 \times 10^9 L_{\odot}$ . While it shows an elongated morphology, it’s unclear if this corresponds to an early-type galaxy or a disc structure. It shows evidence of emission lines of H $\alpha$ , H $\beta$ , and OII, so it is likely a star-forming disc galaxy (SDSS SkyServer 2024;

Lintott et al. 2011). Its redshift of  $z = 0.083082$  and projected distance of 350 kpc makes it a Malin 1 satellite candidate, that may have interacted in the past (Reshetnikov et al. 2010). This interaction could explain the formation of the extended low surface brightness (LSB) disc or serve as a catalyst for the emergence of the suspected stream B (Galaz et al. 2015). Additionally, the zoom-in image of eM1 (see point 4 in Fig. 1), shows that the peak of the surface brightness is shifted from the geometrical center. This off-centre, found in this study, could indicate that exo-Malin 1 has experienced past interactions that could involve Malin 1. Further discussion on this can be found in the Section 5. Moreover, it is very intriguing that eM1 appears to align on the sky with the stream B along an almost straight line towards the center of Malin 1.

- 5 Malin 1B (M1B): Reshetnikov et al. (2010) recognized it as a galaxy interacting with Malin 1 (point 5 in Fig. 1). Furthermore, Saha et al. (2021) identified its interaction specifically with the central area of Malin 1, implying it might be responsible for initiating recent star formation in the galaxy (Saha et al. 2021). The possibility that stream A is concurrently connected with Malin 1B (Reshetnikov et al. 2010) and/or Malin 1A (Saburova et al. 2022) supports the hypothesis of a past merger. Malin 1A and Malin 1B, both compact ellipticals (cE) (Saburova et al. 2022), could have experienced tidal stripping, potentially explaining their compact nature. If further stripping occurs, they might evolve into objects similar to ultra-compact dwarfs (UCDs), as suggested by Bekki et al. (2001). Moreover, such tidal shaping of satellite galaxies has been shown to operate on mass scales of magnitudes of orders of difference (Blaña et al. 2025). Meanwhile, Malin 1C’s classification remains unclear: it could be either a UDG (Ji et al. 2021) or a young star-forming region (Junais et al. 2024), possibly linked to past interactions.
- 6 Malin 1A (M1A): identified as another compact elliptical (cE), typically located close to larger galaxies and prone to tidal interactions and stripping (Saburova et al. 2022; Johnston et al. 2024). M1A has undergone significant tidal encounters with Malin 1, leading to the depletion of nearly all their gas (Kim et al. 2020).
- 7 Cavity: A cavity in the southern region of the observed LSB disc indicates a reduced stellar density, displaying an apparent gap between spirals. Furthermore, irregularities in the HI gas distribution observed in the HI data are also noted (Lelli et al. 2010). Its origin is unknown: it could be the result from a local gas depletion, dust extinction, or satellite interactions.
- 8 Galaxy SDSS J123657.22+142021.1 is a background galaxy at a high redshift ( $z = 0.364$ ) beyond Malin 1, and a broad-line galaxy (Abazajian et al. 2009).
- 9 HII regions: Identified using VLT-MUSE, such as the one highlighted by a yellow ellipse, indicate recent star formation activity (Junais et al. 2024).
- 10 Malin 1C (M1C): is reported as an star forming (H $\alpha$ ) blob candidate using VLT-MUSE observations (Junais et al. 2024), with signatures of H $\alpha$  emission and at a redshift similar to Malin 1 ( $z = 0.08292$ ). It is positioned at a projected distance of 46.75 kpc from Malin 1, forming part of the Malin 1 surroundings. Fig. 1 shows a color-enhanced image of M1C. MUSE H $\alpha$  emission line has a relative mean velocity of 54 km/s from Malin 1 systemic velocity, being likely bound to Malin 1 and with a velocity dispersion higher than 90 km/s Junais et al. (2024, private communication). This

Table 2: Line of sight Velocity  $V_{los}$ , and related properties of *Malin 1* and associated galaxies

Galaxy <sup>a</sup>	$V_{los}$ [km/s] <sup>b</sup>	Petrosian radius [kpc] <sup>g</sup>	Luminosity [ $L_{\odot}$ ] <sup>h</sup>	$\gamma_{band}$ [ $M_{\odot}/L_{\odot}$ ] <sup>n</sup>	$M_{\star}$ [ $M_{\odot}$ ] <sup>q</sup>
M1	$0 \pm 1$ <sup>c</sup>	$5.6 \pm 0.2$	$(1.07 \pm 0.06) \times 10^{11}$ <sup>i</sup>	$(3.3 \pm 0.4)$ <sup>i</sup>	$(1.4 \pm 0.3) \times 10^{11}$ <sup>r</sup>
eM1	$132 \pm 37$ <sup>d</sup>	$5.2 \pm 0.4$	$(5.6 \pm 0.3) \times 10^9$ <sup>d</sup>	$(0.9 \pm 0.2)$ <sup>p</sup>	$(5.0 \pm 0.9) \times 10^9$
M1B	$65 \pm 22$ <sup>d</sup>	$2 \pm 2$	$(2.6 \pm 0.7) \times 10^9$ <sup>d</sup>	$(3.4 \pm 0.6)$ <sup>o</sup>	$(8.8 \pm 1.7) \times 10^9$
M1C	$54 \pm 27$ <sup>e</sup>	$1.5 \pm 0.5$	$(1.3 \pm 0.2) \times 10^8$ <sup>l</sup>	$(0.9 \pm 0.2)$ <sup>p</sup>	$(1.2 \pm 0.3) \times 10^8$
M1A	$54 \pm 27$ <sup>f</sup>	$2 \pm 2$	$(1.12 \pm 0.15) \times 10^9$ <sup>m</sup>	$(3.4 \pm 0.6)$ <sup>o</sup>	$(3.8 \pm 0.7) \times 10^9$

<sup>a</sup> Galaxies abbreviations, defined in Table 5, and in Fig. 1. <sup>b</sup>  $V_{los}$  velocity of the satellite with respect to Malin 1 system. <sup>c</sup> M1 centre with dispersion which comes from the projected angular scale (Galaz et al. 2015). <sup>d</sup> Reported by Reshetnikov et al. (2010). <sup>e</sup> (Junais et al. 2024, and private communication). <sup>f</sup> Our estimation based on both, M1A and M1C having approximately the same distance from the M1 centre. <sup>g</sup> Radius where surface brightness is 20% of the average within it (Petrosian 1976; Psychogyios et al. 2016); data from SDSS SkyServer (2024). <sup>h</sup> This work: averaging  $\gamma_{iso-thermal}$  and  $\gamma_{NFW}$  profiles. <sup>i</sup> UDG in r band (SDSS SkyServer 2024). <sup>m</sup> cE in r band (SDSS SkyServer 2024). <sup>n</sup> Mass to Light ratio in solar units (Bell & De Jong 2001). <sup>o</sup>  $\gamma$  value for cE (Bell & De Jong 2001). <sup>p</sup>  $\gamma$  value for LSB or UDG (Bell & De Jong 2001). <sup>q</sup> Stellar mass. <sup>r</sup> This work: stellar mass estimation within  $r < 100$  kpc, averaging models with ISO and NFW profiles.

high velocity dispersion could also mean that the system corresponds to a dwarf galaxy. Moreover, the nature of H $\alpha$  blobs are still debated, with tidal remnants, stripped clouds, or ultra diffuse galaxies (UDG) as candidates Ji et al. (2021). Moreover, M1C is appears aligned with the stream B, which would be a natural consequence if this is the core of the stream that is being tidally disrupted. Current orbital configurations significantly influence tidal stream arrangements, impacting both the leading and trailing arms, and possibly affecting the remnant bound core. This effect is supported by various simulation studies (see Fig. 1 in Niederste-Ostholt et al. 2012).

### 3. Modelling the Malin 1 system

Here we describe in detail how we model the gravitational potential of Malin 1 and the possible orbits of its satellites and streams. The gravitational potential and orbital models are constrained by observational data, such as the surface brightness profile, rotation curve, and line-of-sight velocities.

#### 3.1. Observational Data and Constraints

For the photometric modelling, we considered different surface brightness (SB) band data observations of Malin 1: *HST/F814W* for the central area, within  $< 15$  kpc (Barth 2007), and the  $r$  and  $g$  bands for the extended disc, reaching  $100 - 120$  kpc in radius (Moore & Parker 2006; Reshetnikov et al. 2010; Saha et al. 2021). In the analysis, we also used the SB profile of the  $R$ -band as explained in Lelli et al. (2010). Analysis was conducted on the HI rotation curve data (Pickering et al. 1997; Lelli et al. 2010), taking into account the stellar, gaseous, and DM mass components. Furthermore, the inner part of the Rotation Curve (RC), dominated by the bulge/core and HSB disc, would be constrained by incorporating existing kinematic data of the central region, such as long-slit spectroscopy (Junais et al. 2020), MUSE observations (Johnston et al. 2024; Junais et al. 2024; Saburova et al. 2022).

In addition, the sky coordinates of the stellar streams, measured with respect to the centre of Malin 1 as the inertial reference frame, were derived from the deep photometric maps of Galaz et al. (2015), who report a  $\sim 200$  kpc stream that extended toward exo-Malin 1. We also carried out a visual inspection of these maps, guided by surface brightness enhancements relative to the background, to select representative coordinates  $x$ - $y$  points along both streams, which were then used as observational constraints in our orbital modelling. The  $x$ -axis aligns with the right

ascension ( $\alpha$ ) and increases leftward on the sky plane. The  $y$ -axis aligns with the declination ( $\delta$ ) and increases northward (upward) in the plane of the sky. The statistical accuracy of each coordinate  $x$  and  $y$  was enhanced by using the projected angular scale and the median seeing of  $0.8$  arcsec (Galaz et al. 2015), given a confidence level of  $\pm 1.25$  kpc. For the distance  $r$  measured from the centre of Malin 1, error propagation was used (see Fig. A.1 and Table A.1).

Moreover, the line of sight velocity of the satellite, with respect to the Malin 1 system, denoted  $V_{los}$  and cited from various sources (Dey et al. 2019; Cook et al. 2023; Reshetnikov et al. 2010; Saburova et al. 2022; Galaz et al. 2015; Junais et al. 2024; Johnston et al. 2024), along with other likelihood-associated satellite galaxies, is listed in Table 2.

#### 3.2. Malin 1 gravitational potential

To investigate the dynamics of the Malin 1 satellites and streams, we need to model the gravitational potential to calculate the orbits. For this, we proceed with the modelling process in two steps.

First, we construct a model of the surface brightness profile of Malin 1 using the photometric data described in Section 3.1. This model represents the main Malin 1 substructures described in Section 2: the bulge/bar and the HSB and LSB discs. We adopted photometric models that offer analytical solutions for their potentials, which allow for quick orbital calculations and a large parameter space exploration. Therefore, we used the Miyamoto-Nagai (MN) model proposed by Miyamoto N. & Nagai R. (1975), where its potential relates to the density through the Poisson equation and is defined as:

$$\Phi_{MN}(R, z) = -\frac{GM}{\sqrt{R^2 + (a + \sqrt{Z^2 + b^2})^2}}, \quad (1)$$

where  $a$  and  $b$  are the radial and vertical scale lengths,  $M$  is the mass,  $R = \sqrt{X^2 + Y^2}$  is the cylindrical radius,  $X, Y, Z$ , and  $r = \sqrt{R^2 + Z^2}$  is the spherical radius. We note that when  $a = 0$ , the potential  $\Phi_{MN}$  simplifies to the Plummer profile (Plummer H. C. 1911). For photometric modelling, we fit the total luminosity of each component  $L_x$ . The luminosity can be converted to stellar mass  $M_{\star} = \gamma_{band} L_{band}$ , where  $\gamma_x$  is the stellar mass-to-light ratio in a band. In our analysis, we used a Plummer profile to model the bulge/bar of Malin 1 and two MN models for the components of the HSB and LSB disc. We also test replacing the spherical bulge model with a triaxial bar model Long & Murali (1992)

Table 3: Definition of parameters used in the orbital modelling for each scenario, described in Table 5.

Parameter	Symbol	Description
Spatial coordinate (los)	$Z$	Line-of-sight distance of the progenitor candidate relative to the mid-plane of Malin 1 (kpc). A positive (negative) value places the object in front of (behind) the disc along the observer's line of sight.
Tangential velocity	$V_{\text{tg}}$	Magnitude of the velocity component perpendicular to the line of sight ( $\text{km s}^{-1}$ ). Together with the observed los velocity, it defines the full 3D velocity vector of the orbit.
Position angle	PA	Angle measured at the orbit initial condition, indicating the direction of the tangential velocity vector in the plane of the sky, measured counterclockwise from north through east (degrees).
Pericenter	$R_{\text{peri}}$	Minimum galactocentric distance to Malin 1 ( $r$ ) reached by the orbit (kpc).
Apocenter	$R_{\text{apo}}$	Maximum distance $r$ to Malin 1 reached by the orbit (kpc).
Eccentricity	$\epsilon$	Orbital shape, defined as $\epsilon = \frac{R_{\text{apo}} - R_{\text{peri}}}{R_{\text{apo}} + R_{\text{peri}}}$ . Circular orbits have $\epsilon = 0$ and highly elongated orbits have 1.
Posterior probability	$\log(p)$	Logarithm of the posterior probability returned by the MCMC sampling. Larger values correspond to orbital solutions that are statistically more significant and better constrained by the observational data.

using Plummer luminosity and scale lengths from [Saha et al. \(2021\)](#), finding similar main orbital properties. Given that the MN profile becomes a Kuzmin profile if a face-on disc is integrated along the LoS ([Binney J. & Tremaine S. 2008](#)), we used this simplified profile to fit the surface brightness profiles.

In the second step, we fitted circular velocity ( $v_c$ ) models to the observed gas kinematics to obtain the mass-related parameters. Here we fit the mass-to-light ratio  $\gamma$  under the maximal disc assumption, which means that the stellar components contribute the maximum possible fraction of the observed rotation curve before the DM halo becomes dominant ([Binney J. & Tremaine S. 2008](#)). For the representation of the dark halo, we implemented two sets of models. One with the Navarro-Frenk-White (NFW) profile ([Navarro et al. 1996](#)), which aligns with the  $\Lambda$ CDM model, and another with a pseudo-isothermal (ISO) profile ([De Blok & Bosma 2002](#)). Both profiles are widely used to describe the density distribution of DM halos, as has been applied to Malin 1 (e.g. [Lelli et al. 2010](#)). NFW assumes that dark matter halos have a characteristic "cuspy" central density and extend over large distances. The ISO profile, on the other hand, features a flat central core, which implies a constant density at the centre ([Mo 2010](#)). These are defined as

$$\Phi_{\text{NFW}}(r) = -\frac{GM_h \ln(1 + r/r_s)}{r} \left[ \ln(1 + c) - \frac{c}{1 + c} \right]^{-1}, \quad (2)$$

$$\Phi_{\text{ISO}}(r) = -4\pi G \rho_0 r_c^2 \left[ \frac{1}{2} \ln \left( 1 + \frac{r^2}{r_c^2} \right) + \frac{r_c}{r} \tan^{-1} \left( \frac{r}{r_c} \right) \right]. \quad (3)$$

The NFW model defines the concentration parameter  $c = r_{200}/r_s$ , the virial radius  $r_{200}$ , where the mean density becomes 200 times the critical density of the Universe, and the scale radius  $r_s$ . On the other hand, in the ISO profile ([De Blok & Bosma 2002](#)), the parameter  $r_c$  defines the radius of the core and  $\rho_0$  indicates the central density of the DM halo.

In addition, Malin 1 has a very extended HI disc component ([Bothun et al. 1987](#); [Pickering et al. 1997](#)). To include this in the gravitational model, we again used a Miyamoto-Nagai model with a mass of  $M_{\text{HI}} = (4 - 7) \times 10^{10} M_{\odot}$  ([Lelli et al. 2010](#)), a scale length of  $a_{\text{HI}} = a_2$ , where we assumed that it has a distribution similar to that of the LSB component and a height of  $z_{\text{gas}} = 0.3$  kpc. Furthermore, factors 1.1 for molecular  $H_2$  and 1.4 for helium gas are included ([Lelli et al. 2010](#)). Together, these components represent the baryonic mass.

### 3.3. Orbital Modelling: Setup, Parameters, and Methodology

Literature studies on the disruption of satellite galaxies and the formation of stellar streams with N-body simulations typically

find that the remaining satellite core has a leading and a trailing component (e.g. [Fellhauer et al. 2006](#); [Smith et al. 2013](#), and references therein). Moreover, satellites and their streams can have different morphologies that depend on the potential of the host and, more importantly, on the eccentricity of the orbit. Very circular orbits can produce ring-like streams or polar ring streams, as observed in the Sombrero galaxy ([Martínez-Delgado et al. 2021](#)). Radial orbits can produce a more diverse morphology depending on the location where the satellite and the streams are observed in their common orbit. For example, a satellite can be preferentially closer to one of its streams, with the trailing stream being closer to the apocentre, and the leading arm could be tidally compressed while entering the host, with the bound core somewhere in the middle of the orbit. (see Fig. 1 in [Niederste-Ostholt et al. 2012](#)).

Our goal is to explore orbital configurations or scenarios that could connect observed stellar streams A and B with the observed satellites in Malin 1, identifying progenitor candidates. Therefore, we are required to consider all detected satellite galaxies near Malin 1 (see Section 2), and to explore the configurations or scenarios that could connect these structures in different ways. Each scenario is also evaluated using two distinct gravitational potentials for Malin 1, the NFW and the ISO DM models (Section 3.2).

For the orbital model of the satellite and stellar streams, we updated the orbital integrator code `DELOREAN` ([Blaña et al. 2020](#)) with the potentials of Malin 1 and coupled it with `EMCEE` ([Blaña et al.](#), in prep.) to reconstruct the orbital trajectories of satellites while fitting the position information of the streams. For this, we maximised the likelihood ( $p = -\log(\chi^2)$ ) given by the chi-squared orbit fitted in projection to the stream sky coordinates, shown in Fig. A.1 and Table A.1. Given that the satellite-to-host mass ratio is small ( $\lesssim 0.1$ ), we model the orbits of the satellites and the streams as test particles, where  $M_{\text{Satellite}}/M_{\text{Malin 1}} < 0.01$ . The input fixed parameters that we introduce in `DELOREAN` are the position of Malin 1 and the positions and line-of-sight velocities ( $v_{\text{los}}$ ) of the satellites and the positions of the streams (see Table A.1). The free parameters in each orbit calculation are the los coordinate  $Z$ , the tangential velocity  $V_{\text{tg}}$ , the position angle PA, and the log posterior  $\log(p)$ . From the posterior sampling, we derive the orbital characteristics: the pericenter  $R_{\text{peri}}$ , the apocenter  $R_{\text{apo}}$ , and the orbital eccentricity  $\epsilon$ , which help us classify the orbital nature and stability of each solution. More details are provided in Table 3.

The selection of parameter ranges in each orbital scenario is based on a combination of observational constraints and iterative modelling; our general strategy involves the following steps:

1. **Observational Data:** We started the process using satellite/stream observational data, specifically the measured projected sky position and line-of-sight velocity for each object.
2. **Initial Parameter Space:** The orbital solution space was explored by fitting three main free parameters: the line-of-sight distance  $z$ , the magnitude of the tangential velocity  $V_{\text{tg}}$ , and the direction of  $V_{\text{tg}}$  is aligned with the position angle PA, defined as the angle measured counter-clockwise from North, centered at satellite's observed position. The ranges of initial parameters were established based on physical motivations to restrict search volume and avoid nonphysical results.
3. **Iterative MCMC Refinement:** An initial EMCEE run uses wide uniform priors to sample the global parameter space. We then iteratively refined the prior ranges based on the most probable values (identified using the CORNER plots) and repeated the MCMC fitting until the posterior distributions and the resulting orbital paths converged to a robust solution.
4. **Orbit Evaluation:** The resulting 3D orbital trajectories were evaluated by checking their consistency against observed features, specifically the stream curvature, direction, and alignment with the disc of Malin 1.
5. **Best-Fit Solution:** The final, converged parameter distributions derived from the iterative fitting represent the optimised orbital solution for the stream or satellite.

## 4. Results

Here, we first present the results of the mass and potential modelling of Malin 1. This is followed by the results of the orbital modelling of the stellar streams and satellites, considering different satellite-stream scenarios.

### 4.1. Mass and potential models for Malin 1

In Fig. 2 (top panel), we display the surface brightness profile of the best Malin 1 luminosity model as a function of galactocentric distance. We also show the data points of the r-band, which were converted from the  $g$  and  $r$  bands (Lelli et al. 2010), revealing a good fit to the main substructures. As expected, the fit produces a Plummer profile that characterises Malin 1's bulge well, while one Miyamoto-Nagai model (Kuzmin) represents the HSB disc, and the extended disc represents the LSB component, dominating the SB beyond 20 kpc. The MCMC-EMCEE posterior distributions of the luminosities and scale-length parameters are shown in Figure 3. The components of the best fitted models are reported in Table 4, resulting in a luminosity of the inner components of  $L_{\text{LSB}} = 3.4 \times 10^{10} L_{\odot}$ , while the LSB component has a luminosity of  $L_{\text{LSB}}(R < 100 \text{ kpc}) = 2.2 \times 10^{10} L_{\odot}$  within the observed radius of  $R \sim 100 \text{ kpc}$ .

Following this, we proceed to model the rotation curve data (RC). For this, we used four HI rotation curve data points taken from Lelli et al. (2010). Additionally, there are recent gas kinematic observations from the central region (Junais et al. 2020; Junais et al. 2024; Johnston et al. 2024). We tested the inclusion of these additional observations, considering 17 points: 10 H $\alpha$ , 3 [OII], and 4 H I (see Fig. A.2). However, the gas kinematics of H $\alpha$  and [OII] appear to be affected by noncircular motions, (Saburova et al. 2022; Kataria & Saha 2025). Including them in the fit would bias the mass models, particularly in the innermost kiloparsecs. A more sophisticated triaxial modelling of the stellar kinematics would be required; however, this would mostly improve the modelling in the central region, which is beyond the scope of this work. For this reason, and to ensure consistency

Table 4: Malin 1 model best-fitted parameters. The results include photometric and gas disk components, stellar mass-to-light ratios ( $\gamma$ ), and Dark Matter (DM) halo parameters for both the ISO and NFW models.

I. Photometric and Gas Model Parameters <sup>a</sup>			
Component	Parameter [Unit]	Value	
Bulge	$r_{\text{Bulge}}$ [kpc]	$1.0 \pm 0.1$	
	$L_{\text{Bulge}}$ [ $10^{10} L_{\odot}$ ]	$1.3 \pm 0.1$	
HSB Disc	$z_{\text{HSB}}$ [kpc]	$0.3^i$	
	$R_{\text{HSB}}$ [kpc]	$4.6 \pm 0.3$	
	$L_{\text{HSB}}$ [ $10^{10} L_{\odot}$ ]	$2.3 \pm 0.1$	
LSB Disc	$z_{\text{LSB}}$ [kpc]	$0.3^i$	
	$R_{\text{LSB}}$ [kpc]	$94^{+7}_{-6}$	
	$L_{\text{LSB}}$ [ $10^{10} L_{\odot}$ ]	$7.1^{+0.6}_{-0.5}$	
Gaseous disc	$z_{\text{Gas}}$ [kpc]	$0.3^i$	
	$R_{\text{Gas}}$ [kpc]	$94^{+7}_{-6}$	
	$M_{\text{Gas}}$ [ $10^{10} M_{\odot}$ ]	$8.5 \pm 1.0^j$	
<b>II. Stellar <math>\gamma</math>:</b>			
	$\gamma_{\text{Bulge}} [M_{\odot} L_{\odot}^{-1}]$	<b>ISO Halo</b> $0.90^{+0.16k}_{-0.16}$	<b>NFW Halo</b> $0.90^{+0.16k}_{-0.16}$
<b>III. DM Halo Parameters:</b>		<b>ISO Halo</b>	<b>NFW Halo</b>
	$R_{\text{vir}}$ [kpc] <sup>b</sup>	$282^{+14}_{-14}$	$231^{+17}_{-15}$
	$M_{\text{vir}}$ [ $10^{12} M_{\odot}$ ] <sup>c</sup>	$2.57^{+0.44}_{-0.38}$	$1.41^{+0.28}_{-0.22}$
	$\rho_0$ [ $10^6 M_{\odot} \text{kpc}^{-3}$ ] <sup>d</sup>	$48.7^{+28.9}_{-28.9}$	$6.72^{+4.77}_{-4.77}$
	$r_c$ [kpc] <sup>e</sup>	$3.67^{+1.73}_{-0.85}$	—
	$r_s$ [kpc] <sup>f</sup>	—	$20.2^{+6.55}_{-6.55}$
	$c^g$	—	$11.4^{+3.8}_{-3.8}$
	$\chi^2_{\text{reduced}}$	1.21	2.15

<sup>(a)</sup> Stellar components modelled with the Miyamoto-Nagai potential (Eq. 1), where  $z_h$  is the scale height,  $R_d$  is the scale length, and  $M_d$  is the mass. <sup>(b)</sup> Virial radius,  $R_{200}$ . <sup>(c)</sup> Virial mass,  $M_{200}$ . <sup>(d)</sup> Central density for the ISO model ( $\rho_0$ ). <sup>(e)</sup> Bulge radius ( $r_c$ ) for the ISO model. <sup>(f)</sup> Scale radius ( $r_s$ ) for the NFW model. <sup>(g)</sup> Concentration parameter  $c = R_{\text{vir}}/r_s$  for the NFW model. <sup>(i)</sup> Parameter fixed during fitting. <sup>(j)</sup> Estimated error based on HI flux uncertainty. <sup>(k)</sup> Fixed value based on stellar population synthesis models Lelli et al. (2010); the quoted uncertainty is the estimated systematic error.

with the large-scale dynamical modelling, we adopted a conservative strategy: we excluded the inner H $\alpha$  and [OII] data and retained only the outermost H $\alpha$  point, together with the four H I points. Thus, our final RC fit is based on five data points from robust tracers (four H I + one H $\alpha$ ), which are less affected by non-circular motions. This approach balances the use of available kinematic constraints with the need to avoid systematics introduced by disturbed central motions.

The RC modelling requires fitting a dark matter ISO or NFW halo model, and converting the luminosities to stellar mass profiles. For the latter, we implemented three independent mass-to-light ratio parameters ( $\gamma$ ): one for the bulge, another for the HSB disc, and a third value for the LSB disc component. Although physically motivated, introducing this amount of free parameters increases the degeneracy when fitting the rotation curve. Therefore, for our fiducial modelling we followed Lelli et al. (2010) and adopted  $\gamma_{\text{LSB}} = 0.90 M_{\odot} L_{\odot}^{-1}$  as a fixed LSB value, and fitted  $\gamma_{\text{Bulge}}$  and  $\gamma_{\text{HSB}}$  for ISO halo models and NFW models. In addition, we chose a prior distribution strongly constrained by color information and stellar population models

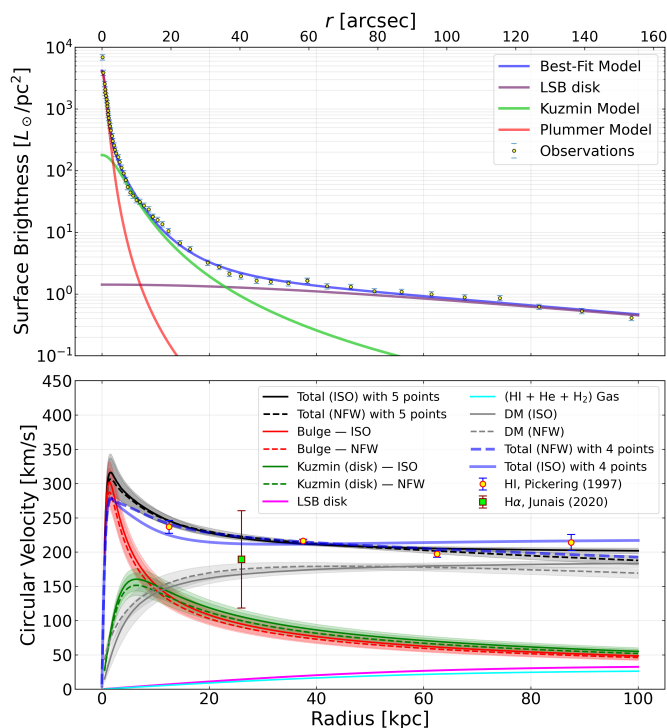


Fig. 2: **Top panel:** The observed  $R$ -band surface brightness profile of Malin 1 as a function of the galactocentric radius (Lelli et al. 2010). Overplotted are the best-fit stellar components: a Plummer model for the bulge (red line), a Miyamoto–Nagai (Kuzmin) disc for the inner HSB component (green line), and another Miyamoto–Nagai disc for the extended LSB component (purple line). The total best-fit photometric model is shown in blue. **Bottom panel:** Observed H I rotation data from Pickering et al. (1997) recalculated in Lelli et al. (2010) (yellow circles) and H $\alpha$  data from Junais et al. (2020) (green square). We show Malin 1 best model fit: the stellar bulge (red), HSB disc (green), and LSB disc (purple), and the gaseous disc H I+He+H<sub>2</sub> (cyan), and with gray curves the DM halo model cases ISO (solid), and NFW (dashed). The black curves show the total mass model cases for the ISO (solid) and NFW (dashed) halos fitting five data points (four H I + one H $\alpha$ ). We also show a test model (blue) fitted to the H I data only adopting a single  $\gamma$  for the HSB disc and bulge. The shaded regions represent the 1 $\sigma$  confidence intervals from the MCMC posteriors.

from Bell & De Jong (2001) and other  $\gamma$  constraints in Malin 1 (Junais et al. 2020). The resulting posterior distribution of the models that used the ISO halo is shown in Fig. 4, and NFW in Fig. C.1. We also tested the degeneracy of  $\gamma_{\text{LSB}}$  by fixing the value of  $\gamma_{\text{Bulge}} \approx 3.8 M_{\odot} L_{\odot}^{-1}$ ,  $\gamma_{\text{HSB}} \approx 1.5 M_{\odot} L_{\odot}^{-1}$  based on previous work (Junais et al. 2020, see their Fig. 9), leaving  $\gamma_{\text{LSB}}$  as a free parameter, obtaining a range  $\approx 0.86\text{--}0.90 M_{\odot} L_{\odot}^{-1}$  in concordance with Lelli et al. (2010). Furthermore, we also tested using a mass-to-light value for the bulge and disc region  $\gamma_{\text{Bulge}} = \gamma_{\text{HSB}} = 3.4 M_{\odot} L_{\odot}^{-1}$ , finding results consistent with Lelli et al. (2010). The best parameters are reported in Table 4, showing  $\gamma$  for each stellar component, along with the corresponding DM halo parameters for both the ISO and NFW models.

In general, we find that the bulge region has systematically higher  $\gamma$  values than the HSB disc component. The rotation curves of the best ISO and NFW models are shown in Figure 2 (bottom panel). The decomposition also shows the contribution

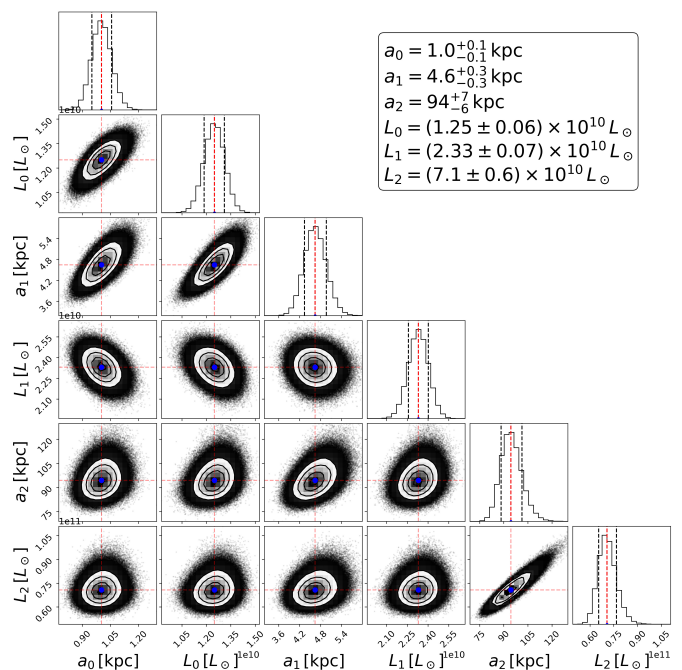


Fig. 3: Parameter posterior distributions for the surface brightness fitting of Malin 1. The scale length parameters  $a_0$ ,  $a_1$ , and  $a_2$ , and luminosities  $L_0$ ,  $L_1$ ,  $L_2$  are the parameters for the Bulge (Plummer), HSB disc (Kuzmin), and the LSB disc (Kuzmin) components. The histograms are the marginalized distributions for each parameter, with the 16th, 50th, and 84th percentiles (vertical dashed lines) and values shown in the legend.

of different mass components: stellar bulge, HSB/LSB discs, and the gaseous disc (HI, He and H<sub>2</sub>). Both the high- and low-surface brightness (HSB and LSB) regions of the disc are considered. The figure further compares the performance of the two halo parameterizations, highlighting the differences between the NFW and ISO models. Figure 3 illustrates the optimized EMCEE fit parameters for the surface brightness model, while Figure 4 shows the equivalent parameters for the rotation curve model. The data compiled for the two profiles is presented in Table 4. The model with the ISO dark matter profile provides better fits of the rotation curve, as shown by the reduced ( $\chi^2$ ) of the MCMC. This is due to the flat rotation curve behaviour of the isothermal profile, while the NFW halo drops faster at the same distances and similar masses. Moreover, we also find that the models with NFW produce higher values of  $\gamma$  than the ISO models. This is due to the cuspy nature of the NFW dark halo model, which introduces more mass in the centre, forcing the stellar mass to have lower  $\gamma$ . This results in NFW halos having virial masses of  $1.4 \times 10^{12} M_{\odot}$  and lower than the ISO models with  $2.6 \times 10^{12} M_{\odot}$ . Furthermore, our test with equal central  $\gamma$  result in more massive ISO halo models with  $3.7 \times 10^{12} M_{\odot}$ .

Given that the differences between the potential models with ISO and NFW haloes are larger than the differences within each halo model profile, we proceed to use both sets of models to consider the uncertainties in the potential that are used to explore the orbital scenarios in the following section.

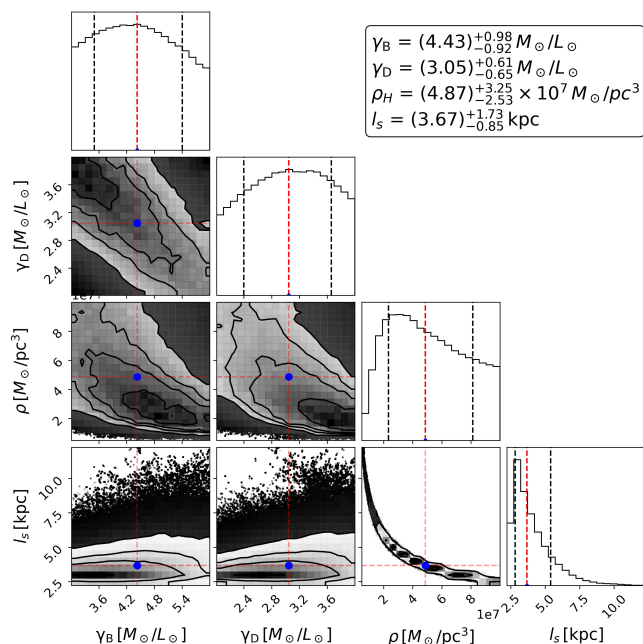


Fig. 4: Posterior distributions of the mass-to-light ratios for the bulge, HSB disc, and the ISO DM halo parameters: central density  $\rho_{\text{Halo}}$  and the core radius  $r_c$ . Diagonal panels show the marginalized distributions with the 16th, 50th, and 84th percentiles indicated by dashed lines. Contour plots display parameter covariances. The legend reports the best-fit values with  $1\sigma$  uncertainties. The ISO model provides robust fits, with maximum-a-posteriori values (blue points) close to the medians.

#### 4.2. Scenarios connecting possible progenitor satellite candidates and stellar streams

Our goal is to search for orbital solutions of satellite galaxies that can overlap with the stellar streams. From these we focus on radial orbits that reach the central regions of Malin 1 where the satellites could have experienced the most intense tidal forces. We also considered polar orbital solutions, similar to those observed in the Sombrero galaxy (Martínez-Delgado et al. 2021), where the satellite has near circular orbits while being tidally stripped.

We defined five scenarios that depend on what satellite is assumed to be the progenitor, and two subcases (a and b) that depend on what combinations of the streams are assumed to be associated with each satellite. These are summarized in Table 5. For many scenarios and cases, we found radial and polar orbital solutions. In addition, we tested two different DM potentials (NFW and ISO) for each scenario.

Following our procedure to constrain the regions where the best orbits are found (see Section 3.3), we converge to the parameter ranges reported in Table B.1 and Table B.2 where we justify each. Table 6 reports the Best-fit posterior probabilities ( $p$ ) for all the scenario models. The investigation consists of millions of orbits per scenario, resulting in a comprehensive analysis of  $\sim 130$  million orbits in total to explore the parameter space. Here, we highlight the solutions that most accurately correspond to the observational data and adhere to physical constraints, such as having bounded orbital solutions. However, unbound solutions were also found. Here, we proceed to describe each scenario in detail:

In the following, we discuss each scenario and the main orbital properties obtained from the modelling. In general, we managed to identify orbital solutions that have a radial behav-

Table 5: Scenarios defining orbital configurations that connect a specific satellite galaxy as the progenitor candidate for a single or both streams (cases a and b). Scenario V assumes that the stream is the disrupted progenitor. Each scenario has been evaluated using two halo models (NFW and ISO). Abbreviations: M1 = Malin 1, sA = Stream A, sB = Stream B, eM1 = Exo-Malin 1, M1A = Malin 1A, M1B = Malin 1B, M1C = Malin 1C.

Scenario	Case	Combinations
I	a	<b>eM1 + sB</b>
	b	<b>eM1 + sA + sB</b>
II	a	<b>M1C + sB</b>
	b	<b>M1C + sA + sB</b>
III	a	<b>M1B + sB</b>
	b	<b>M1B + sA + sB</b>
IV	a	<b>M1A + sA</b>
	b	<b>M1A + sA + sB</b>
V	a	<b>sA</b>
	b	<b>sB</b>

ior, and orbits with a more circular morphology that due to the satellite configurations produce polar-like orbital solutions perpendicular to Malin 1 LSB disk. Furthermore, we identified scenarios where the orbital solutions that are gravitationally bound (I-a, II-a, II-b, IV-a, and V-a), and unbound (I-b, III-a, III-b, IV-b, and V-b). These correspond to the following:

#### – Scenario I-a (Radial and Polar): **eM1 + sB**.

We constrain the current tangential velocity of the candidate progenitor **eM1** by computing various orbits backward in time. The stellar stream **sB** appears spatially connected to the central region of **M1** and the offset position of **eM1** (as initially noted by its position relative to labels 3 and 4 in Fig. 1). Figure 5 left panel illustrates the posterior distributions for the orbital parameters of **Scenario I-a**, showing the  $1\sigma$  uncertainties derived from the MCMC samples. Figure 6 illustrates two representative solutions of Scenario I-a: (a) a radial orbit (using the ISO DM potential) and (b) a polar orbit (using the NFW DM potential). The uncertainty bands  $1\sigma$  shown in the temporal and kinematic evolution panels (iii and vi) were derived from 300 MCMC samples. **Radial Orbit:** The best-fit radial orbit, integrated over  $[-13.0, 20.0]$  Gyr, demonstrates a close passage consistent with the formation of **sB** as the trailing tidal segment of **eM1**. The pericenter passage occurred at  $P \approx 33$  kpc at  $T_p \approx -1.6$  Gyr, with a velocity of  $|V_p| \approx 548$  km/s. This orbit yields a large line-of-sight velocity variation ( $\Delta V_{\text{LoS}} \approx 650$  km/s), which is consistent with the velocity spread expected for a plunging orbit. This solution reveals that **eM1** could be a backslash satellite with a long orbital period. N-body simulations have shown that depending on satellite and stream location along the orbit, the leading or trailing streams can be stretched or diluted along the orbit producing apparent gaps between the satellite and the stream (e.g. Smith et al. 2013). Future follow-up deeper observations and simulations will further investigate this scenario. **Polar Orbit:** The best-fit polar orbit, utilizing the NFW potential, links **eM1** and **sB** via a more distant pericenter:  $P \approx 147$  kpc at  $T_p \approx -2.4$  Gyr, with  $|V_p| \approx 318$  km/s. Despite the larger pericenter, the orbit's alignment is still consistent with **sB** being the trailing component of **eM1**. The lower  $\Delta V_{\text{LoS}} \approx 350$  km/s is characteristic of the shallower tidal interaction experienced in the cuspy NFW potential. Both Scenarios I-a Radial and Polar, are statistically viable

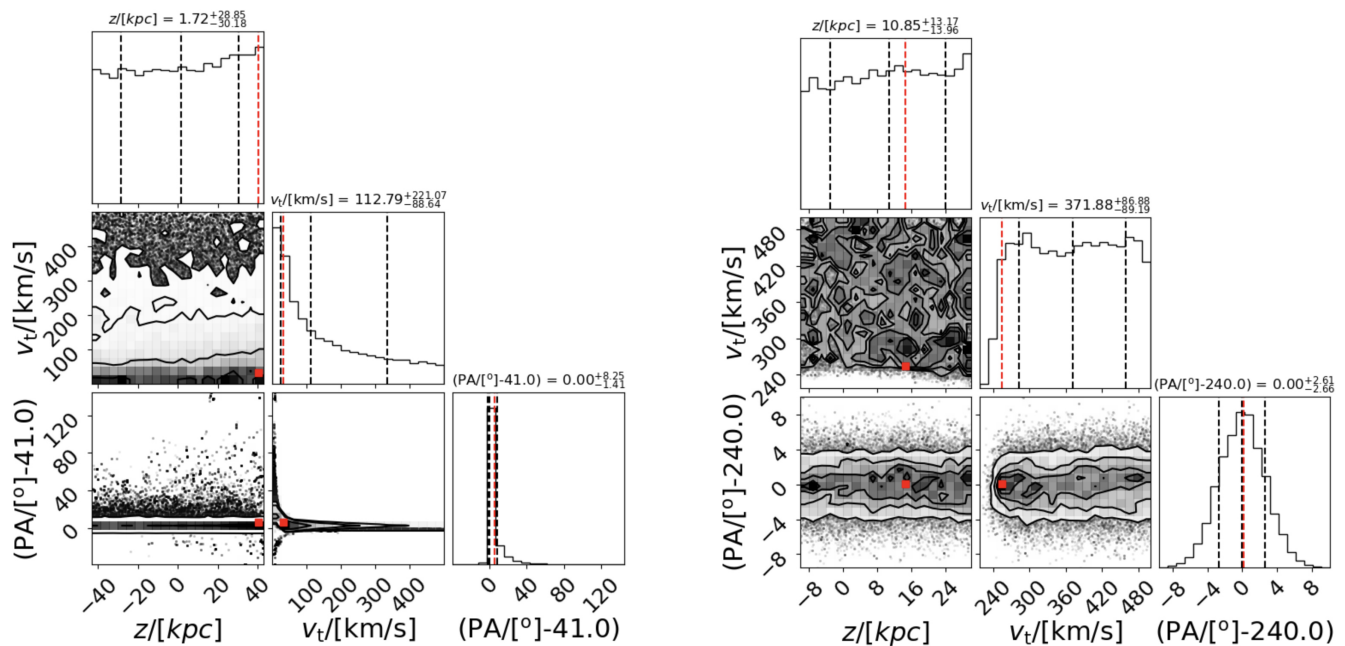


Fig. 5: Corner plots of the posterior distributions of orbital parameters ( $z$ ,  $v_t$ , and PA offset) obtained with *emcee*. **Left:** Scenario I-a (radial orbit, ISO halo). **Right:** Scenario IV-a (polar orbit, ISO halo). Diagonal panels show marginalized 1D distributions with dashed lines marking the median and  $1\sigma$  uncertainties. Off-diagonal panels show 2D covariances with 68% and 95% confidence regions. These two scenarios illustrate contrasting orbital families (radial vs. polar) within the ISO halo parametrization.

solutions, with Scenario I-a Polar offering a higher posterior probability, as discussed in detail in Section 4.3.

– Scenario I-b: **eM1 + sB + sA.**

In our search for a radial orbit that could simultaneously fit both streams, a solution was not possible. Instead, we found a highly eccentric orbit that apparently is **unbound** from **Malin 1**. The pericentric passage is elevated, occurring at **694 kpc** with a velocity of **933 km/s**, which happened **500 Myr** ago. This high-energy orbit (shown in panel i) of Fig. D.1) suggests that the progenitor **eM1** is currently escaping the gravitational potential of **Malin 1**.

– Scenario II-a: **M1C + sB.**

This scenario explores **M1C** as the progenitor of **sB**, suggesting that **sB** contains stellar remnants and potentially undetected gas once linked to **M1C**. The probable orbit, shown in panel (a) Fig. 7 and integrated over  $[-2.9, 2.3]$  Gyr, experienced its pericenter passage approximately **0.2 Gyr** ago. **Key Finding:** The orbit is **bound** (as seen in the distance-time plot) and polar to **Malin 1**. It exhibits a moderate dynamic interaction, with line-of-sight velocities reaching  $\Delta V_{\text{los}} \approx 400$  km/s. This bound outcome is in agreement with the successful bound solution found in Scenario **II-b**.

– Scenario II-b: **M1C + sA + sB.**

This setup explores a crucial dynamical link: the possibility that both stellar streams, **sA** and **sB**, may be composed of stellar remnants originating from a single progenitor, the companion **M1C**. This model assumes a highly tidally disruptive system where the leading and trailing arms of the progenitor connects both streams, as suggested by previous numerical studies of satellite galaxy tidal evolution (e.g. Niederste-Ostholt et al. 2012). Figure 7 shows the best-fit radial orbit solution, integrated over  $[-2.0, 3.5]$  Gyr using the

preferred **ISO DM potential**. **Key Findings:** This is the **only solution found** that successfully links two separate streams (**sA** and **sB**) via a common progenitor (**M1C**). The orbit is highly radial and plunges deep into the Malin 1 potential well. The model predicts an extremely close **pericenter passage at  $P \approx 3$  kpc**, occurring **2.8 Gyr** in the leading component ( $T_L$ ). The current position of **M1C** places it on this highly energetic orbit, with a predicted pericenter velocity of  $V_p \approx 598$  km/s. The temporal evolution (Fig. 7, panel iii) indicates that the stream **sA** is linked to an earlier passage of **M1C** approximately **0.33 Gyr** ago, while stream **sB** is associated with the subsequent passage. This scenario requires significant tidal stripping due to the very small pericenter radius.

– Scenario III-a: **M1B + sB.**

We investigate the possibility that **M1B** is the progenitor of the stellar stream **sB**. The best-fit orbit, shown in Panel iv), Fig. D.1, suggests a highly eccentric association ( $\epsilon \sim 0.88$ ) with a pericenter of  $P \sim 7$  kpc and a velocity of  $|V| \sim 707$  km/s occurring  $\sim 0.01$  Gyr ago. **Key Finding:** This close, high-velocity encounter is dynamically possible but results in an **unbound** orbit, making it dynamically disfavored as the progenitor.

– Scenario III-b: **M1B + sB + sA.**

This situation seeks **M1B** as the progenitor for both **sB** and **sA** simultaneously. **Key Finding:** It was not possible to find a single fitting orbit to connect both streams, and the best solution found was an apparently **unbound** orbit, which is shown in panel ii) of Fig. D.1. The pericenter passage occurred relatively recently, **20 Myr** ago, at **32 kpc** with a very high velocity of  $\sim 705$  km/s.

– Scenarios IV-a: **M1A + sA** and V-a: **sA.**

We explore two distinct possibilities for the origin of stellar

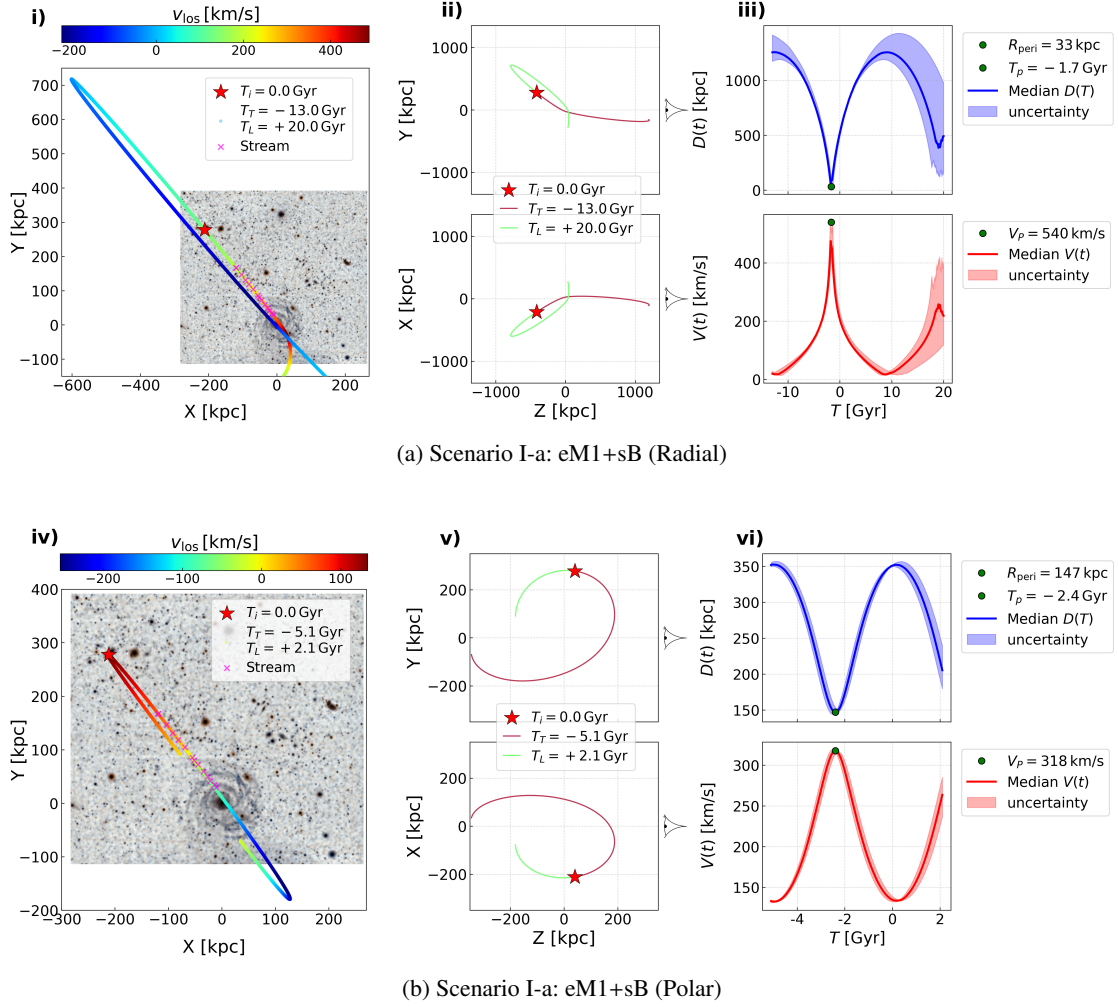


Fig. 6: Best-fit integrated orbits for the eM1+sB model, comparing the two highest-likelihood orbit classes: (a) Scenario I-a (Radial) and (b) Scenario I-b (Polar). The uncertainty bands in panels (iii) and (vi) were derived from the 300 mcmc samples with the highest posterior values. **Spatial Projections (Panels i and iv):** The integrated orbit (colored line) is overlaid on the optical image of Malin 1 and its environment (Galaz et al. 2015). The orbit is color-coded by the line-of-sight velocity ( $v_{\text{los}}$ ). The red star marks the progenitor (eM1) at  $T_i = 0.0$  Gyr (present), and the magenta cross denotes stellar stream markers (sB). The  $T_T$  (Trailing) and  $T_L$  (Leading) stream times are marked with dots along the orbit. **Orbital Projections (Panels ii and v):** The Z-Y and Z-X orbital planes are shown for the orbits. The origin  $X, Y = (0, 0)$  kpc is the Malin 1 center. The observer is conceptually located to the right (positive Z and X directions, as indicated by the eye icon). The legends indicate the Trailing ( $T_T$ ) and Leading ( $T_L$ ) integration times and colours used for the orbit segments. **Temporal and Kinematic Evolution (Panels iii and vi):** The top sub-panels show the orbital distance  $D(t)$  (blue) and the bottom sub-panels show the velocity  $V(t)$  (red) as a function of time  $T$ . The solid line is the median orbit, and the shaded regions indicate the  $1\sigma$  uncertainty. The green circle marks the maximum a posteriori pericenter (distance  $R_{\text{peri}}$  and time  $T_p$ ) and pericenter velocity ( $V_p$ ), determined as the median of the extrema across all mcmc samples. **Scenario-Specific Parameters: I-a (Radial, ISO DM):** Best orbit integrated over  $[-13.0, 20.0]$  Gyr. Pericenter passage:  $R_{\text{peri}} \approx 33$  kpc at  $T_p \approx -1.6$  Gyr, with  $|V_p| \approx 540$  km/s. Max  $\Delta V_{\text{Los}} \approx 650$  km/s.  $z \sim -412$  kpc,  $v_t \sim 153$  km/s, PA  $\sim 40^\circ$ , apocenter  $R_{\text{apo}} \sim 1194$  kpc and eccentricity  $\epsilon \sim 0.68$ . This orbit is consistent with sB being the trailing part of eM1. **I-b (Polar, NFW DM):** Best orbit integrated over  $[-5.1, 2.1]$  Gyr. Pericenter passage:  $R_{\text{peri}} \approx 147$  kpc at  $T_p \approx -2.4$  Gyr, with  $|V_p| \approx 318$  km/s. Max  $\Delta V_{\text{Los}} \approx 350$  km/s.  $z \sim -40$  kpc,  $v_t \sim 33$  km/s, PA  $\sim 47^\circ$ , apocenter  $R_{\text{apo}} \sim 354$  kpc and eccentricity  $\epsilon \sim 0.09$ . This orbit, which assumes an NFW DM profile, is also consistent with sB being the trailing part of eM1.

stream sA: first, that its progenitor, M1A, is still a visible component (Scenario IV-a), and second, that the progenitor was completely tidally disrupted, leaving only sA as a remnant (Scenario V-a) (Deason et al. 2023; Panithanpaisal et al. 2021). Figure 8 illustrates the best-fit orbits for both cases. **Scenario IV-a: M1A as Progenitor (Fig. 8, up panels).** The best-fit orbit, integrated over  $[-1.4, 1.7]$  Gyr and characterised by low eccentricity ( $\epsilon \sim 0.08$ ), successfully connects M1A with the observed leading and trailing segments

of sA. **Key Finding:** This represents a tight polar solution for the M1A progenitor, with the first passage occurring 1.4 Gyr ago at a pericenter of approximately  $P \sim 15$  kpc, resulting in a maximum line-of-sight velocity variation of  $\Delta V_{\text{los}} \approx 400$  km/s along the orbit. This scenario establishes a kinematic link between M1A and sA. **Scenario V-a: Disrupted Progenitor (Fig. 8, bottom panels).** This hypothesis models sA as the remnant of a completely destroyed progenitor. The best-fit orbit, integrated on  $[-1.3, 0.7]$  Gyr, re-

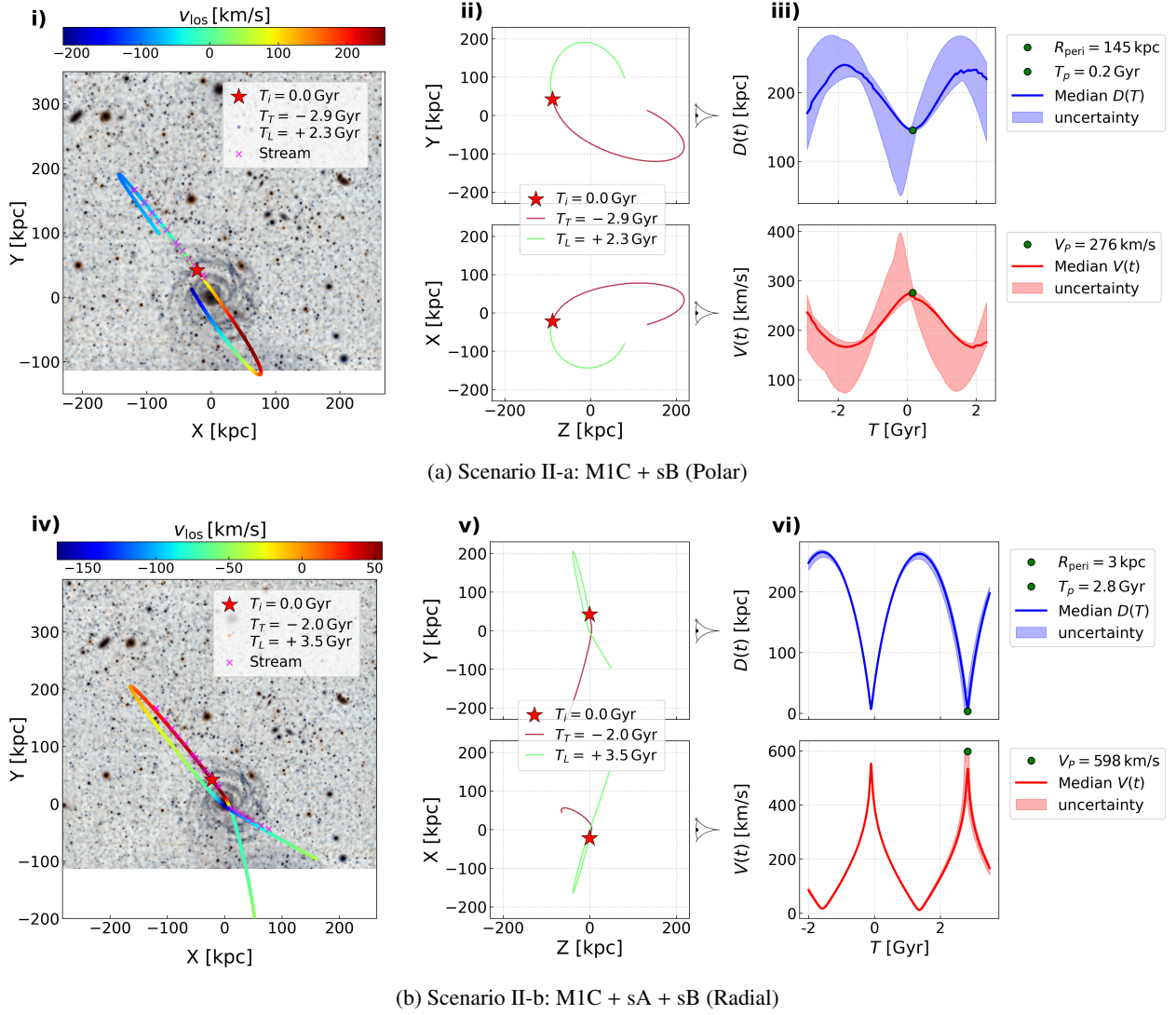


Fig. 7: Best-fit integrated orbits for the progenitor **M1C** and two scenarios. **Panel (a)** corresponds to **Scenario II-a (M1C + sB)** in panels i), ii), and iii). **Panel (b)** corresponds to **Scenario II-b (M1C + sA + sB)** in panels iv), v), and vi). The uncertainty bands (iii, vi) use the 300 highest-posterior MCMC samples. **Panels i and iv (Spatial)**: Integrated orbit (color-coded by  $v_{\text{los}}$ ) overlaid on Malin 1’s optical image. The red star is the progenitor (**M1C**) at  $T_i = 0$ , and the magenta cross marks stream components. **Panels ii and v (Orbital)**:  $Z - Y$  and  $Z - X$  orbital planes. The observer is to the right (positive  $Z$  and  $X$ ). **Panels iii and vi (Evolution)**: Top: orbital distance  $D(t)$  (blue); Bottom: velocity  $V(t)$  (red). The green circle marks the maximum a posteriori pericenter ( $R_{\text{peri}}, T_p$ ) and velocity ( $V_p$ ) from the MCMC sample extrema. **Scenario-Specific Parameters: II-a (M1C+sB, Radial, ISO DM)**: Integrated over  $[-2.9, 2.3]$  Gyr.  $R_{\text{peri}} \approx 145.0$  kpc at  $T_p \approx 0.2$  Gyr,  $|V_p| \approx 276$  km/s. Apocenter  $R_{\text{apo}} \sim 250$  kpc and eccentricity  $\epsilon \sim 0.82$ . This solution is **unbound** and dynamically disfavored. **II-b (M1C+sA+sB, Radial, ISO DM)**: Integrated over  $[-2.0, 3.5]$  Gyr.  $R_{\text{peri}} \approx 3.0$  kpc at  $T_p \approx 2.8$  Gyr,  $|V_p| \approx 598$  km/s.  $R_{\text{apo}} \sim 1530$  kpc and eccentricity  $\epsilon \sim 0.56$ . The leading pericenter passage occurred 2.9 Gyr ago (first passage) and 0.33 Gyr ago (leading arm/second passage). Significantly, this is the only solution found that dynamically links two separate streams (sA and sB) via a common progenitor (M1C).

quires the progenitor to have undergone an extremely close pericenter passage, occurring 1.2 Gyr ago at  $P \sim 3$  kpc with a high velocity of  $|V_p| \approx 493$  km/s. **Key Finding:** The extremely small pericenter strongly supports the possibility of complete tidal disruption. Intriguingly, the proximity of the solutions (similar time frames and dynamics) suggests that the orbital characteristics of sA are strongly constrained by the streams regardless of the progenitor’s current status (intact M1A vs. destroyed progenitor).

– Scenario IV-b: M1A + sA + sB.

This situation posits M1A as the single progenitor for both

stream sB and stream sA. **Key Finding:** It was not possible to find a single fitting orbit to connect both streams simultaneously. Moreover, the best solution found was an apparently **unbound** orbit, which is shown in panel iii), Fig. D.1. This high-energy orbit had a pericenter passage 0.1 Gyr ago at 24 kpc with a velocity of  $\sim 814$  km/s.

– Scenario V-b: sB (Disrupted Progenitor).

We investigate the possibility that sB’s progenitor has been completely destroyed by the tidal forces of Malin 1 (Deason et al. 2023; Panithanpaisal et al. 2021). The results are shown in panel v), Fig. D.1. The required passage to

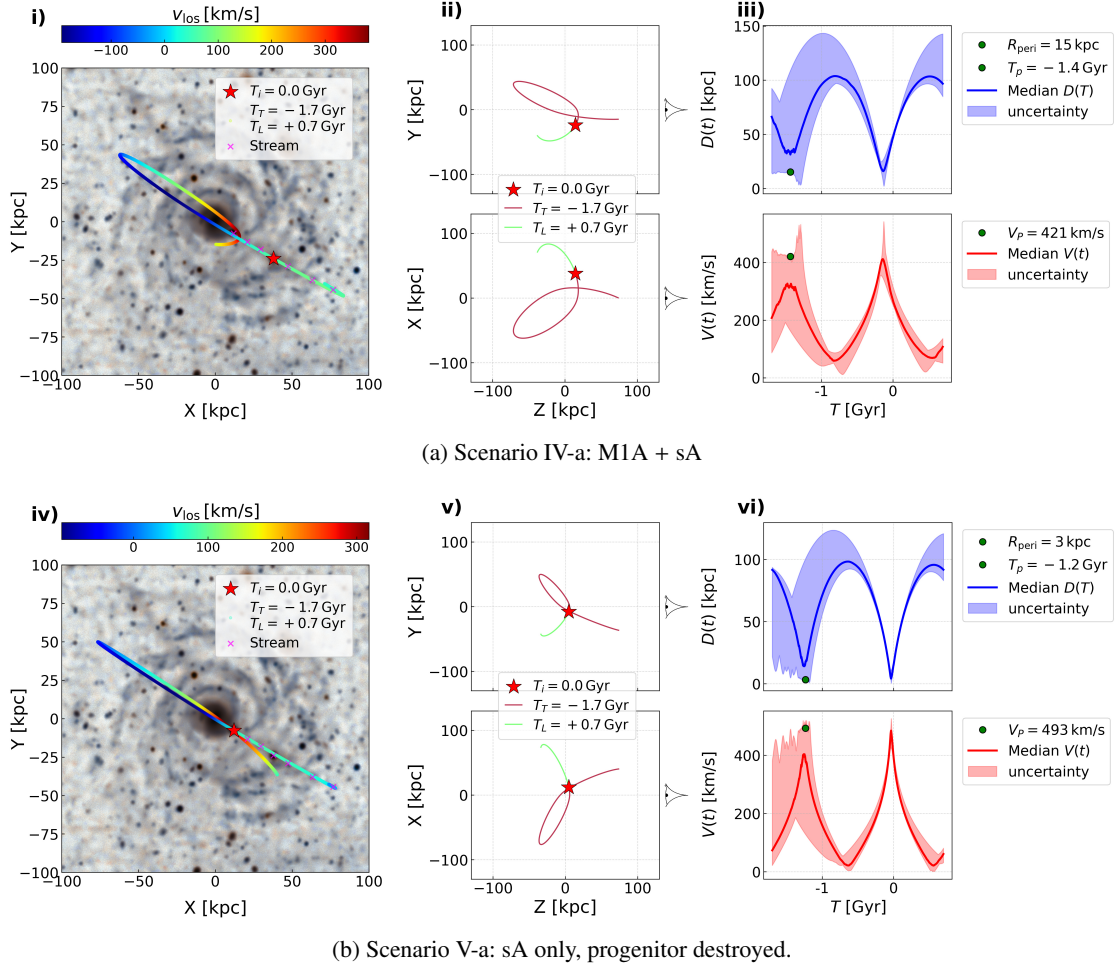


Fig. 8: Best-fit integrated orbits for the stream sA, comparing the two most likely scenarios: (a) Scenario IV-a (M1A progenitor, ISO DM) and (b) Scenario V-a (sA progenitor destroyed, NFW DM). The  $1\sigma$  uncertainty bands in panels (iii) and (vi) were derived from 300 MCMC samples. **Spatial Projections (Panels i and iv):** The integrated orbit (colored line) is overlaid on the optical image of Malin 1. The orbit is color-coded by the line-of-sight velocity ( $v_{\text{los}}$ ). The red star marks the progenitor (M1A/sA) at  $T_i = 0.0$  Gyr (present), and the magenta cross denotes the stellar stream (sA). The  $T_T$  (Trailing) and  $T_L$  (Leading) stream times are marked with dots. **Orbital Projections (Panels ii and v):** The Z-Y and Z-X orbital planes are shown. The origin X, Y = (0, 0) kpc is the Malin 1 center. The observer is conceptually located to the right (positive Z and X directions, as indicated by the eye icon). The legends indicate the Trailing ( $T_T$ ) and Leading ( $T_L$ ) integration times and colours used for the orbit segments. **Temporal and Kinematic Evolution (Panels iii and vi):** The top sub-panels show the orbital distance  $D(t)$  (blue) and the bottom sub-panels show the velocity  $V(t)$  (red) as a function of time  $T$ . The solid line is the median orbit, and the shaded regions indicate the  $1\sigma$  uncertainty. The green circle marks the maximum a posteriori defined pericenter (distance  $R_{\text{peri}}$  and time  $T_p$ ) and pericenter velocity ( $V_p$ ), determined as the median of the extrema across all MCMC samples. **Scenario-Specific Parameters: IV-a (M1A+sA, Polar, ISO DM):** Best orbit integrated over  $[-1.7, 0.7]$  Gyr. Pericenter passage:  $R_{\text{peri}} \approx 15$  kpc at  $T_p \approx -1.4$  Gyr, with  $|V_p| \approx 421$  km/s. Max  $\Delta V_{\text{LoS}} \approx 400$  km/s. This represents a tight polar orbit for the M1A progenitor. **V-a (sA only, Radial, NFW DM):** Best orbit integrated over  $[-1.7, 0.7]$  Gyr. Pericenter passage:  $R_{\text{peri}} \approx 3$  kpc at  $T_p \approx -1.2$  Gyr, with  $|V_p| \approx 493$  km/s. Max  $\Delta V_{\text{LoS}} \approx 400$  km/s. This model shows a very close radial passage that leads to the complete destruction of the progenitor (sA). The proximity of the solutions (same time frame, similar velocities/geometry) suggests that the orbital characteristics of sA are strongly constrained by the streams regardless of the progenitor’s current status (M1A intact vs. sA destroyed).

generate **sB** has a eccentric  $\epsilon \sim 0.60$ , occurring **33 Myr** ago, with a pericenter of **P**  $\sim 11$  kpc and a high velocity of  $D \sim 916$  km/s. **Key Finding:** This small pericenter strongly indicates that complete tidal disruption is plausible. Intriguingly, the current position and trajectory of the modelled stream **sB** in this scenario point dynamically towards the position of the other progenitor candidate, **eM1**.

For a complete visualisation of the unbound solutions, see **Appendix D**.

### 4.3. Evaluating orbital solutions

We illustrate three representative posteriors in the main text, chosen to span both halo parameterizations (ISO and NFW) and two orbital families (polar and radial). The strongest evidence for the origin of **Malin 1** streams comes from models dominated by the **ISO** (cored) Dark Matter halo, which features slightly more frequently among the top-ranked posterior probabilities (Table 6). To illustrate the spectrum of successful fits, we highlight three representative solutions.

Table 6: Best-fit posterior probabilities ( $p$ ) for all modeled scenarios, categorized by orbital configuration and Dark Matter (DM) halo model. Solutions are sorted by decreasing posterior probability. The column B/U denotes the gravitational status of the best-fit orbit: **B** for Bound and **U** for Unbound.

Scenario	Orbit	B/U	DM Model	$\log(p)$	$p$
I-a	Polar	B	ISO	-0.0934	0.911
IV-a	Polar	B	ISO	-0.1057	0.900
V-a	Radial	B	NFW	-0.1056	0.900
V-b	Radial	U	ISO	-0.1166	0.888
V-a	Radial	B	ISO	-0.1216	0.886
I-a	Radial	B	ISO	-0.1226	0.885
III-a	Radial	U	NFW	-0.1319	0.877
IV-a	Polar	B	NFW	-0.1528	0.858
III-a	Radial	U	ISO	-0.1564	0.855
I-a	Polar	B	NFW	-0.1769	0.838
II-a	Polar	B	ISO	-0.2471	0.781
I-a	Radial	B	NFW	-0.2895	0.749
II-b	Radial	B	ISO	-3.0291	0.048
II-b	Radial	B	NFW	-4.4240	0.012

- Scenario I-a, Polar, ISO:** This case provides the **statistically strongest evidence** among all solutions ( $\log p = -0.0934$ ,  $p \approx 0.911$ ) and produces a clean posterior distribution with a narrow position angle (PA). **Key Finding:** This demonstrates the high viability of **polar orbits** when modelling the interaction of **eM1** and **sB** within a **cored halo** potential.
- Scenario IV-a, Polar, ISO:** With  $\log p = -0.1057$  ( $p \approx 0.900$ ), this solution is slightly less statistically favoured but achieves a more radial plunge. **Key Findings:** In a cored halo, this radial increase offsets the weaker inner density slope, yet still yields enough tidal stripping at pericenter to generate Stream A (**sA**).
- Scenario V-a, Radial, NFW:** Our baseline disruption solution, statistically related to Scenario IV-a ( $\log p = -0.1056$ ,  $p \approx 0.900$ ), has a small pericenter ( $R_p \approx 9$  kpc) and  $V_p \approx 437$  km s<sup>-1</sup>. **Key Finding:** In a **cuspy (NFW) halo**, such close high-velocity conditions strongly favor the necessary tidal stripping to explain the complete disruption of the progenitor and are highly consistent with the observed Stream A (**sA**).

We conducted a thorough orbital analysis that spans a wide **40** model combination, covering the full spectrum of physically plausible configurations for Dark Matter (DM) halos (cusp versus core) and orbital geometries (polar versus radial). Although Table 6 catalogues only the best-fit posterior probabilities ( $p$ ) discovered during our search, the solutions presented encompass the most representative and dynamically relevant scenarios. We focus on this subset of solutions, as they successfully reproduce the observed stream track and line-of-sight velocity gradient, including complex cases where a single progenitor is fitted to multiple data sets. This is the Scenario II-b case, in which we used two different sets of data that could be the cause of a small posterior probability (see Table 6).

Using both NFW and ISO DM models, we found that bound orbital solutions were more likely under the ISO profile. This is supported by our maximum likelihood analysis, where the ISO model yielded systematically higher log-likelihood values in both the radial and polar scenarios, see Table 6. This outcome likely arises because the ISO profile predicts a more extended

mass distribution at large radii (Fig. 2, bottom panel), which better accommodates the gravitational constraints required by the satellite orbits. These findings are consistent with the results of (Lelli et al. 2010), who also uses ISO profiles to fit rotation curves, despite the general similarities with NFW-based models.

In Bayesian terms, the values  $\log(p)$  reported in Table 6 represent the logarithm of the posterior probability, combining the likelihood of the model with the prior distributions. Since we maintained consistent prior choices across both the ISO (cored) and NFW (cusped) Dark Matter halo models, the systematic trend toward higher  $\log(p)$  values for the ISO halo solutions reflects a quantitatively better fit to the available kinematic and spatial data. This evidence strongly suggests that a cored DM profile is more compatible with the observed orbital solutions of the Malin 1 streams.

It is important to note that the posterior probabilities in Table 6 depend on the specific data sets used to constrain the models. For example, scenarios in which the progenitor must simultaneously satisfy the constraints of two distinct data sets, such as **Scenario II-b (M1C + sA + sB)**, incur a significant penalty in their marginalized likelihood, which is reflected in a lower overall  $\log(p)$ . Despite this statistical demerit, such solutions are of high physical significance, as they demonstrate the orbital ability of a single progenitor to reproduce multiple stellar features.

## 5. Discussion

### 5.1. Satellite galaxies and stellar streams.

Studies have shown a possible connection between the tidal formation and evolution of cE satellites and their host spiral galaxy, such as M32 and the Andromeda galaxy stream (Ibata et al. 2004; Fardal et al. 2006). This supports the hypothesis that the cE satellites M1A, M1B, and possibly M1C, could also be identified as progenitors of streams A and B as they are tidally processed. Similar findings have been reported for other galaxies, for instance the giant galactic tail *Kite*, which extends over more than 350 kpc (Zaritsky et al. 2023), and the previously mentioned  $\sim 500$  kpc giant stream in the Coma cluster (Román et al. 2023). Both features support the presence of such large-scale streams.

In our study, we identify, among others, a possible orbital solution that connects almost linearly in projection the stream sB with eM1 and Malin 1. Moreover, the central region of eM1 appears off-centre (Fig. 1 - point 4), with an ongoing star formation, which would be naturally explained if it had a fly-by through Malin 1. Such phenomena are often observed in galaxies that undergo gravitational interactions, resulting in an off-centre core or a lopsided disc (Mao et al. 2021). Moreover, we are able to identify radial and polar orbital configurations for eM1. The radial configuration (panel i, Fig. 6) had a  $\sim 33$  kpc pericenter passage  $\sim 1.6$  Gyr ago, being now moving away from Malin 1. More interestingly, the apocenter of this orbit happened 13 Gyr ago, implying that this satellite could be on its first infall. We also estimated that the Jacobi tidal radius of eM1 at the pericenter was between  $\sim 9 - 12$  kpc depending on the stellar and dark matter range. This would again naturally explain the observed internal disturbed morphology. Conversely, the polar configuration reaches a more distant pericenter of 150 kpc, resulting in larger tidal range radii ( $\sim 30 - 70$  kpc) and suggesting only mild tidal stripping. Furthermore, while polar configurations have been observed in systems like the Sombrero galaxy (Martínez-Delgado et al. 2021), the radial interaction is physically analogous to the dramatic tidal stripping seen in the M31-

M32 system (Fardal et al. 2006). Consequently, the radial orbit represents a more efficient mechanism for fueling the observed stellar streams and establishing eM1 as the primary progenitor of the sB stellar component.

We also identify another polar-like orbital solution perpendicular to Malin 1 disk, where M1A could be connected to sA (scenario IV-a, panel a) in Fig. 8). In this arrangement, the orbital solution is also radial having an apocenter of  $\sim 100$  kpc and a pericenter of  $\sim 16.1 \pm 1.2$  kpc that could have impacted Malin 1 disks, providing a possible trigger mechanism for the active star formation observed in Malin 1 (Lelli et al. 2010; Junaïs et al. 2024; Junaïs et al. 2025), and in the central region (Johnston et al. 2024; Kataria & Saha 2025). We note that here we assumed that sA extends along its orbit. Another possibility is that sA could be a tidal arm structure stretching from M1A and aligned towards Malin 1 center following the Lagrange points. Given that our simplistic orbital analysis cannot reproduce these tidal structures, we leave this for a follow-up N-body study. Furthermore, our attempts to connect the satellite M1B with the streams sA and sB (Scenarios III-a/-b) resulted in unbound solutions due to the satellite’s LoS velocity and position near Malin 1 center, which forces it to have large tangential velocities to reach the streams orbital paths.

The satellite M1C appears to be a H $\alpha$  blob (Junaïs et al. 2024, <sup>1</sup>). In (Ji et al. 2021) they propose that blobs in general could be tidal remnants or even progenitors of Ultra Diffuse Galaxies (UDGs), which could be supported by M1C’s observed high H $\alpha$  velocity dispersion ( $\sim 90$  km s<sup>-1</sup>). We found orbits that could connect M1C to the streams, including an interesting case that connects both streams simultaneously (panel (a) of Fig. 7). This solution offers a compelling solution already seen in other galactic systems, and would imply that the complete stream (panel (b) of Fig. 7) could be even longer, extending 500 kpc long at least.

We explored orbital scenarios where we assume that the stellar streams are the disrupted progenitors themselves, as seen in other systems (Deason et al. 2023; Panithanpaisal et al. 2021). In scenarios V-a and V-b we identify possible radial orbital solutions for the streams sA and sB, which could imply recent tidal disruptions. However, solution V-b produces an unbound orbit. We note that in the solution V-a the stream sA appears disconnected from sB, suggesting that it is an independent event. Moreover, the spatial proximity of M1A, sA and M1B also suggests a complex interaction between Malin 1 and this subgroup of satellites.

Finally, we also identified unbound orbital solutions. For example, we attempted to connect eM1 with both stellar streams simultaneously, finding only unbound solutions, as shown by the best-fit trajectories for this configuration (Fig. D.1, panel i). Similar unbound trajectories arise across multiple configurations, including (M1B, sA, sB), (M1A, sA, sB), (M1B, sB), and the sB-only case, as illustrated in panels ii) through v) of Fig. D.1. These unbound solutions could suggest that the mass distribution of Malin 1 is inconsistent with the kinematic states of the satellites, implying that Malin 1 could be more massive than we can estimate by the rotation curve alone. Consequently, given that  $\Lambda$ CDM galaxy formation models show that galaxies are unlikely to have such orbits (e.g. Knebe et al. 2011), we exclude these specific orbital configurations as viable evolutionary paths, implying that the observed stellar streams are likely the result of more constrained, bound accretion events rather than fast unbound encounters.

## 5.2. Satellite interactions and Malin 1 gLSB evolution.

Recent high-resolution observational studies of Malin 1 have revealed a complex dynamics and star formation history (Galaz et al. 2015, 2022, 2024; Johnston et al. 2024; Junaïs et al. 2025; Kataria & Saha 2025), suggesting an active past involving mergers or accretion. Studies have shown in general that examining the formation of tidal streams could provide insight into the timing of major merger events in the main host galaxy (e.g. Martínez-Delgado et al. 2023). Galaz et al. (2024) reported evidence of ongoing star formation (SF) in regions of extremely low molecular gas density, while Johnston et al. (2024) identified a possible double nucleus, pointing towards a recent disturbance or merger. This central activity is further supported by the H $\alpha$  emission studies by Junaïs et al. (2024) and by the presence of high non-circular motions (Kataria & Saha 2025). Within this framework, our semi-analytical orbital analysis explores a wide set of configurations involving Malin 1, the two stream candidates sA and sB, and at least four satellite galaxies —M1A, M1B, M1C, and eM1—and consistently recovers kinematic signatures that corroborate these high velocity encounters.

These non-circular motions are often attributed to recent events such as stellar feedback and satellite accretion (Saburova et al. 2021). Our derived orbital velocities (e.g.,  $V_{tg} = 100 - 700$  km/s for many scenarios, see Table B.1) are high enough to naturally explain the observed non-circular motions in the inner H $\alpha$  and [OII] components discussed by Kataria & Saha (2025), suggesting that the system’s current high-velocity dispersion could be a direct consequence of these high-speed encounters considered in our models.

The observed state of Malin 1 likely reflects a multi-stage assembly process consistent with recent cosmological simulations. For example, Zhu et al. (2018) found a Malin 1 simulated analogue that formed of large diffuse galactic disc driven by the stimulated hot halo gas accretion and the accretion of a pair of intruding gas-rich galaxies in a coherent plane, as found in other simulated gLSBs (Zhu et al. 2023). Our orbital analysis offers a compelling candidate for this process: the temporal coincidence of the eM1 radial passage ( $\sim -1.6$  Gyr) and the M1A encounter ( $\sim -1.4$  Gyr) suggests that these satellites may have acted as intruding galaxies as found in Zhu et al. (2018). This sequential interaction likely catalyzed the dynamical disturbance and subsequent gas inflow necessary to form the observed stellar streams and support the expansive growth of the disc. Consequently, we propose that the morphological state of Malin 1 is the observational legacy of this merger-driven accretion event, which occurred between approximately 1.4 and 1.6 Gyr ago.

The morphological inspection of Malin 1 LSB disk reveals a rich complexity, where we can specifically identify an optical cavity (Fig. 1, Point 7). Additionally, HI observations reveal a warp in the extended gaseous disk, as well as a substructure near the cavity (Pickering et al. 1997; Lelli et al. 2010). Simulations reveal that these types of features can be produced by gravitational interactions with satellite galaxies (e.g. Block et al. 2006; Gordon et al. 2006; Kalberla & Kerp 2009; Kim et al. 2014). Our orbital models indicate that these features are kinematically consistent with recent high-velocity encounters. Our orbital models for M1C reveal two distinct dynamical pathways that explain these structures: a polar configuration (Scenario II-a) with a large pericenter ( $\sim 145$  kpc), which aligns with empirical warp models (Binney 2024), and a radial disc-crossing configuration (Scenario II-b) with a tight pericenter ( $\sim 3$  kpc) approximately 0.2 Gyr ago. This recent radial passage provides the gravitational tide strength necessary to drive the formation

<sup>1</sup> private communication

of the observed stellar streams (sA and sB) and the central disc cavity, positioning M1C as a primary progenitor for these features. Furthermore, the radial encounter of eM1, which occurred  $\sim 1.6$  Gyr ago with a pericenter of  $\sim 33$  kpc, provides a compelling explanation for the larger-scale HI warp and the current kinematic state of the outer disc. Given that the rotation periods in the outer disk are very slow, the cavity at  $R \sim 50$  kpc is around  $T_\theta = 2\pi R/v_c \sim 1.6$  Gyr. Therefore, the cavity could have already rotated around Malin 1 since the eM1 passage. However, independent of the impactor, we identify the cavity as a potential observational fossil substructure produced in an impulsive gravitational encounter.

## 6. Conclusions and future work

In this study, we have performed a comprehensive analysis of the stellar streams and satellite surrounding the giant low-surface-brightness galaxy (gLSBG) Malin 1. For this we combined deep  $R$ -band photometry with HI and  $H\alpha$  kinematics to determine the gravitational potential of Malin 1 to model the orbital dynamics of its satellites to search for orbital solutions that can connect them with the observed stellar streams sA and sB (Galaz et al. 2015). Our key findings are summarized as follows:

1. Massive dark matter halo: we confirm that Malin 1 is hosted by a massive dark matter halo (Section 4.1). The MCMC modeling of the rotation curve yields a virial mass of  $M_{\text{vir}} = 1.4^{+0.3}_{-0.2} \times 10^{12} M_\odot$  for an NFW profile and  $M_{\text{vir}} = 2.6 \pm 0.4 \times 10^{12} M_\odot$  for a pseudo-isothermal profile. The latter provides a statistically better fit to the outer rotation curve data.
2. Connecting satellite orbits with streams: using our orbital models, we identified viable orbital solutions that we call scenarios (Section 4.2) connecting the satellite galaxy candidates M1A, M1B, M1C, and eM1 to the observed stellar streams. These are:
  - (a) Malin 1 interacting with satellite M1A provides a bound orbital configuration, identifying M1A as a plausible progenitor for the stellar stream sA.
  - (b) Interaction models involving satellite M1B suggest that it is a candidate progenitor for the streams; however, the resulting orbits are unbound or marginally bound implying high-velocity encounters.
  - (c) The orbital connection between satellite M1C and stream sB can be modelled via a polar configuration. We also identify a radial orbital solution that allows to simultaneously connect streams sA and sB with M1C (Fig. 7), which would imply that the stream is more extended than currently observed.
  - (d) We identify two types of orbits that can connect the distant eM1 satellite with sB, finding radial and polar configurations (Fig. 6). Both solutions result in long orbital periods, with the radial solution allowing stronger tidal interaction with Malin 1 and indicating that eM1 would be on its first infall.

These results indicate that while several satellites could be progenitor candidates of the observed streams and tidal debris, their specific interaction properties (e.g. pericenters, bound vs. unbound) vary significantly across the system.

3. Types of orbital interactions: Our modeling reveals two distinct modes of satellite interaction categorized by orbital geometry and pericentric proximity:
  - (a) **Close Radial Encounters:** These represent high-impact trajectories characterized by small pericenters. Notable

examples include the M1C-driven interaction (driving sA and sB) and the sA-only event both occurring at  $\sim 3$  kpc as found by Johnston et al. (2024); Kataria & Saha (2025), as well as the M1A-driven interaction at  $\sim 15$  kpc and the eM1 radial encounter at  $\sim 33$  kpc. These close-range crossings generate the impulsive gravitational forcing necessary to trigger significant tidal stripping and drive the observed morphological evolution of the Malin 1 disc.

- (b) **Distant Polar Orbits:** In contrast, we also identify possible polar orbital configurations, similar to the ones observed in the Sombrero galaxy (Martínez-Delgado et al. 2021). These solutions involve the satellites eM1 or M1C connected with the stream sB, and exhibit larger pericenters of  $\sim 145$ – $147$  kpc. These solutions imply weaker interactions with Malin 1's outer halo rather than a direct crossing events with the HSB/LSB disc components.

The findings of this work provide a viable dynamical framework for understanding the role of "nurture" in the evolution of giant LSBGs. To further refine this history, future work will focus on:

- Spectroscopic analysis: Upcoming MUSE and JWST data will be utilized to determine the metallicities and star formation histories of the streams and M1C. This will help distinguish between tidal debris and *in-situ* star-forming regions (e.g.,  $H\alpha$  blobs).
- Simulations: The orbital parameters derived in this study will serve as initial conditions for full N-body hydrodynamical simulations. These will investigate the long-term survival of the streams and the origin of the observed warp and cavity in the outer disc.
- Environmental survey: A broader analysis of the 1 Mpc environment around Malin 1 will clarify the impact of the local cosmic web on the galaxy's continued growth and satellite accretion history (Bustos-Espinoza et al. in prep.).

These dynamical interactions likewise offer a solid basis for interpreting the recent star formation history of Malin 1. The impulsive gravitational encounters found in our models—especially those characterized by small-pericenter radial passages—are highly effective at driving gas inflows and concentrated star formation, in agreement with recent observational work (Galaz et al. 2022, 2024; Johnston et al. 2024; Kataria & Saha 2025). This implies that the observed central activity and irregular star-forming patches are not random, but instead arise directly from satellite-driven gas compression and tidal perturbations.

Ultimately, this study shows that the environment of Malin 1 is complex and it could result of multiple satellite tidal interactions, providing a key benchmark for the role of hierarchical assembly in the evolution of giant low-surface-brightness galaxies.

*Acknowledgements.* This paper is part of a Ph.D. thesis. The primary author expresses gratitude for support received from the ANID BASAL project CATA FB210003 and Pontificia Universidad Católica de Chile (PUC), as well as access to the Horus and Geryon 2 PUC servers. Support was also received from the Organization of American States (OAS) for the 2021-2022 scholarship and from the Sociedad Chilena de Astronomía (SOCHIAS) through two grants under the Prof. Adelina Gutiérrez program. Furthermore, the author acknowledges support from the Carrera de Física at the Instituto de Investigaciones Físicas, Universidad Mayor de San Andrés (UMSA) in La Paz, Bolivia, and is grateful to the Indian Institute of Astrophysics for a six-week visit, including the Vainu-Bappu Observatory, in early 2025. This research was also supported by the Asociación Boliviana para el Avance de la Ciencia (ABAC) and

Sociedad Boliviana de Física (SOBOFI). MD and SB acknowledge the support of the Science and Engineering Research Board (SERB) Core Research Grant CRG/2022/004531 and the Department of Science and Technology (DST) grant DST/WIDUSHI-A/PM/2023/25(G) for this research. The authors (RBE, GG, and MB) acknowledge the support of the European Southern Observatory (ESO) for providing space for discussions while this paper was written. GG thanks Fondecyt Regular 1230231. GG thanks Pontificia Universidad Católica de Chile, ESO, France-Chile Laboratory of Astronomy (FCLA), and Laboratoire d'Astrophysique de Marseille (LAM) for their support during a 2024-2025 sabbatical leave. J. is funded by the European Union (MSCA EDUCADO, GA 101119830 and WIDERA ExGal-Twin, GA 101158446). THP acknowledges support from the Agencia Nacional de Investigación y Desarrollo (ANID) grant CATA-Basal FB210003. This research has used the NASA/IPAC Extragalactic Database (NED), which is operated by the Jet Propulsion Laboratory, California Institute of Technology, under contract with the National Aeronautics and Space Administration. This research has made use of NASA's Astrophysics Data System Bibliographic Services.

## References

- Abazajian, K. N., Adelman-Mccarthy, J. K., Agüeros, M. A., et al. 2009, *Astrophysical Journal, Supplement Series*, 182, 543
- Bannikova, E. Y. 2018, *MNRAS*, 476, 3269
- Barth, A. J. 2007, A NORMAL STELLAR DISK IN THE GALAXY MALIN 1 I, Tech. rep.
- Bekki, K., Couch, W. J., & Drinkwater, M. J. 2001, *ApJ*, 552, L105
- Bell, E. F. & De Jong, R. S. 2001, STELLAR MASS-TO-LIGHT RATIOS AND THE TULLY-FISHER RELATION, Tech. rep.
- Binney, J. 2024
- Binney J. & Tremaine S. 2008
- Blair, W. P., Long, K. S., Winkler, P. F., Lacey, C. K., & Williams, B. F. 2019, The Fireworks Galaxy, NGC 6946: Looking at the Fading Embers, Tech. rep.
- Blaña, M., Burkert, A., Fellhauer, M., Scharfmann, M., & Alig, C. 2020, *MNRAS*, 497, 3601
- Blaña, M., Fellhauer, M., Smith, R., et al. 2015, *MNRAS*, 446, 144
- Blaña, M., Puzia, T. H., Ordenes-Briceno, Y., et al. 2025, *A&A*, 699, A69
- Block, D. L., Bournaud, F., Combes, F., et al. 2006, *Nat*, 443, 832
- Boissier, S., Boselli, A., Ferrarese, L., et al. 2016, The properties of the Malin 1 galaxy giant disk: A panchromatic view from the NGVS and GUViCS surveys, Tech. rep.
- Bonaca, A., Naidu, R. P., Conroy, C., et al. 2021, *ApJ Letters*, 909, L26
- Bothun, G. D., Impey, C. D., Malin, D. F., & Mould, J. R. 1987, DISCOVERY OF A HUGE LOW-SURFACE-BRIGHTNESS GALAXY: A PROTODISK GALAXY AT LOW REDSHIFT?, Tech. Rep. 1
- Bustos Espinoza, R. O. E., Galaz, G., & Blaña, M. 2024a, in 32nd General Assembly International Union (IAUGA 2024), 2541
- Bustos Espinoza, R. O. E., Galaz, G., & Blaña, M. 2024b, in AAS/Division of Dynamical Astronomy Meeting, Vol. 55, AAS/Division of Dynamical Astronomy Meeting, 405.20
- Cook, D. O., Mazzarella, J. M., Helou, G., et al. 2023, *ApJ Supplement Series*, 268, 14
- Das, M. 2013, Giant Low Surface Brightness Galaxies: Evolution in Isolation, Tech. rep.
- De Blok, W. J. & Bosma, A. 2002, *A&A*, 385, 816
- Deason, A. J., Koposov, S. E., Fattahi, A., & Grand, R. J. 2023, *MNRAS*, 520, 6091
- Dey, A., Schlegel, D. J., Lang, D., et al. 2019, *AJ*, 157, 168
- Di Teodoro, E. M., Posti, L., Fall, S. M., et al. 2023, *MNRAS*, 518, 6340
- Disney, 1976
- Du, W., Cheng, C., Zheng, Z., & Wu, H. 2020, *AJ*, 159, 138
- Fardal, M. A., Babul, A., Gehean, J. J., & Guhathakurta, P. 2006, *MNRAS*, 366, 1012
- Fellhauer, M., Evans, N. W., Belokurov, V., et al. 2006, Is Ursa Major II the Progenitor of the Orphan Stream?, Tech. rep.
- Foreman-Mackey, D., Hogg, D. W., Lang, D., & Goodman, J. 2012
- Freeman, K. C. 1970, ON THE DISKS OF SPIRAL AND SO GALAXIES, Tech. rep.
- Galaz, G., Frayer, D. T., Blaña, M., et al. 2022, *ApJ Letters*, 940, L37
- Galaz, G., González-López, J., Guzmán, V., et al. 2024
- Galaz, G., Milovic, C., Suc, V., et al. 2015, *ApJ*, 815, L29
- Gerritsen, J. P. E. & De Blok, W. J. G. 1999, Star formation and the interstellar medium in low surface brightness galaxies III. Why they are blue, thin and poor in molecular gas, Tech. rep.
- Gordon, K. D., Bailin, J., Engelbracht, C. W., et al. 2006, *ApJ*, 638, L87
- Hoffman, Y., Silk, J., & Wyse, R. F. G. 1992, THE FORMATION OF GIANT LOW SURFACE BRIGHTNESS GALAXIES, Tech. rep.
- Ibata, R., Chapman, S., Ferguson, A. M., et al. 2004, Taking measure of the Andromeda halo: A kinematic analysis of the giant stream surrounding M31
- Impey, C. & Bothun, G. 1997, LOW SURFACE BRIGHTNESS GALAXIES, Tech. rep.
- Ji, X., Li, C., Yan, R., et al. 2021, *MNRAS*, 508, 3943
- Johnston, E. J., Galaz, G., Blaña, M., et al. 2024, *A&A*, 686
- Junais, Boissier, S., Epinat, B., et al. 2020, *A&A*, 637
- Junais, Ruiz Cejudo, I., Guerra Arencibia, S., et al. 2025, *Astronomy & Astrophysics*, 702
- Junais, Weibacher, P. M., Epinat, B., et al. 2024, *A&A*, 681
- Kalberla, P. M. & Kerp, J. 2009, Annual Review of A&A, 47, 27
- Kataria, M. & Saha, K. 2025, arXiv e-prints, arXiv:2511.12177
- Kazantzidis, S., Moore, B., & Mayer, L. 2004, in *Astronomical Society of the Pacific Conference Series*, Vol. 327, *Satellites and Tidal Streams*, ed. F. Prada, D. Martinez Delgado, & T. J. Mahoney, 155
- Kim, J. H., Peirani, S., Kim, S., et al. 2014, *ApJ*, 789 [arXiv:1406.6074v1]
- Kim, S., Jeong, H., Rey, S.-C., et al. 2020, *ApJ*, 903, 65
- Knebe, A., Libeskind, N. I., Doumler, T., et al. 2011, *MNRAS*, 417, 56
- Lelli, F., Fraternali, F., & Sancisi, R. 2010
- Lintott, C., Schawinski, K., Bamford, S., et al. 2011, *MNRAS*, 410, 166
- Long, K. & Murali, C. 1992, *ApJ*, 397, 44
- Maeda, F., Egusa, F., Ohta, K., et al. 2022, *ApJ*, 926, 96
- Mao, Y.-Y., Geha, M., Wechsler, R. H., et al. 2021, *ApJ*, 907, 85
- Mapelli, M., Moore, B., Ripamonti, E., et al. 2008, *MNRAS*, 383, 1223
- Martínez-Delgado, D., Cooper, A. P., Román, J., et al. 2023, *A&A*, 671, A141
- Martínez-Delgado, D., Román, J., Erkal, D., et al. 2021, *MNRAS*, 506, 5030
- Miro-Carretero, J., Gomez-Flechoso, M. A., Martínez-Delgado, D., et al. 2024
- Miyamoto N. & Nagai R. 1975
- Mo, 2010, *Galaxy Formation and Evolution*, Tech. rep., Cambridge
- Moore, L. & Parker, Q. A. 2006, *Publications of the Astronomical Society of Australia*, 23, 165
- Navarro, Frenck, & White. 1996
- Niederste-Ostholt, M., Belokurov, V., & Evans, N. W. 2012, *MNRAS*, 422, 207
- Noguchi, M. 2001, *MNRAS*, 328, 353
- Ogle, P. M., Lanz, L., Appleton, P. N., Helou, G., & Mazzarella, J. 2019, *ApJ Supplement Series*, 243, 14
- Ogle, P. M., Lanz, L., Nader, C., & Helou, G. 2016, *ApJ*, 817, 109
- Panithanpaisal, N., Sanderson, R. E., Wetzell, A., et al. 2021, *ApJ*, 920, 10
- Peñarrubia, J., Mconnachie, A., & Babul, A. 2006, ON THE FORMATION OF EXTENDED GALACTIC DISKS BY TIDALLY DISRUPTED DWARF GALAXIES, Tech. rep.
- Petrosian, V. 1976, SURFACE BRIGHTNESS AND EVOLUTION OF GALAXIES, Tech. rep.
- Pickering, T. E., Impey, C. D., Van Gorkom, J. H., & Bothun, G. D. 1997, NEUTRAL HYDROGEN DISTRIBUTIONS AND KINEMATICS OF GIANT LOW SURFACE BRIGHTNESS DISK GALAXIES, Tech. rep.
- Plummer H. C. 1911
- Psychogios, A., Charmandaris, V., Diaz-Santos, T., et al. 2016, *A&A*, 591
- Reshetnikov, V. P., Moiseev, A. V., & Sotnikova, N. Y. 2010
- Román, J., Rich, R. M., Ahvazi, N., et al. 2023, *A&A*, 679
- Saburova, A., Chilingarian, I., Kasparova, A., et al. 2022, in *Astronomy at the Epoch of Multimessenger Studies*, 395-397
- Saburova, A. S., Chilingarian, I. V., Kasparova, A. V., et al. 2021, *MNRAS*, 503, 830
- Saburova, A. S., Chilingarian, I. V., Kulier, A., et al. 2023, *MNRAS: Letters*, 520, L85
- Saha, K., Dhiwar, S., Barway, S., Narayan, C., & Tandon, S. 2021, *Journal of Astrophysics and Astronomy*
- Salinas, V. H. & Galaz, G. 2021, *ApJ*, 915, 125
- SDSS SkyServer. 2024, SkyServer DR18
- Smith, R., Fellhauer, M., Candelish, G. N., et al. 2013
- Vera-Casanova, A., Gómez, F. A., Monachesi, A., et al. 2022, *MNRAS*, 514, 4898
- Zaritsky, D., Crossett, J. P., Jaffé, Y. L., et al. 2023, *MNRAS*, 524, 1431
- Zhu, Q., Pérez-Montaño, L. E., Rodríguez-Gomez, V., et al. 2023, *MNRAS*, 523, 3991
- Zhu, Q., Xu, D., Gaspari, M., et al. 2018, *MNRAS: Letters*, 480, L18

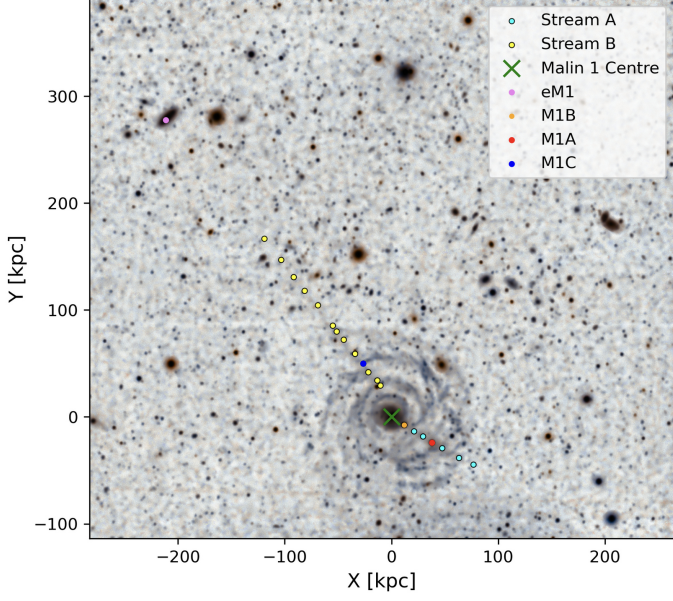


Fig. A.1: Stream points, sA (cyan points) and sB (yellow points), and four satellites, M1A (red), M1B (orange), M1C (blue), and eM1 (violet). The center of Malin 1 is marked with a green cross. Data values are shown in Table A.1.

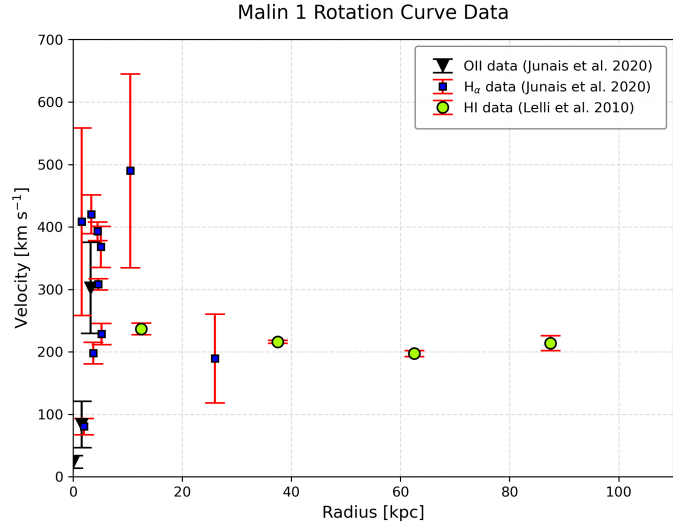


Fig. A.2: Observed Malin 1 rotation curve including HI, OII, and  $H\alpha$  data.

## Appendix A: Stream Points

Table A.1 presents the Stream Points used as prior information for the Monte Carlo Markov chain MCMC-EMCEE method (Foreman-Mackey et al. 2012), identified visually from Fig. 1 (Galaz et al. 2015).

## Appendix B: Priors and Ranges

Table B.1 defines each orbital parameter: line-of-sight coordinate  $z$ , tangential velocity  $V_{tg}$ , position angle PA, pericenter, apocenter, eccentricity  $\epsilon$ , and posterior log-probability. The physical motivation for the parameter ranges is also explained.

## Appendix C: MCMC Parameter Fits

### C.1. NFW halo

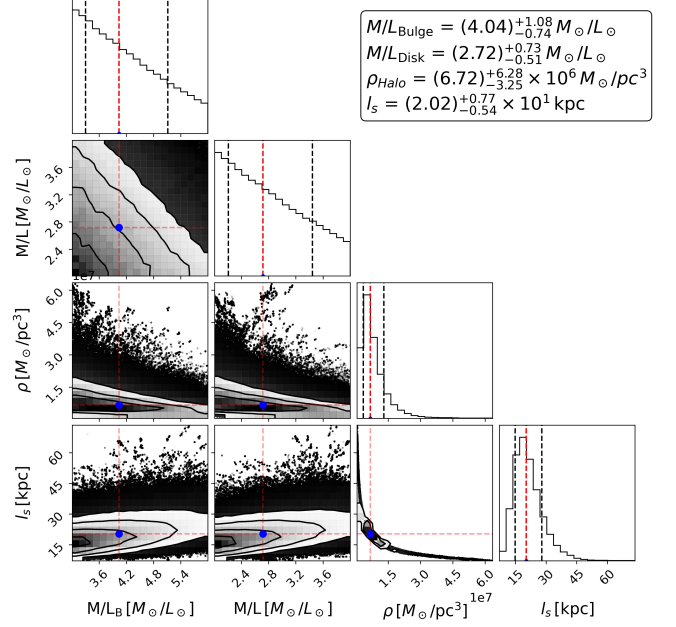


Fig. C.1: Posterior distributions of the mass-to-light ratios for the bulge and HSB disc, together with the NFW DM halo parameters (central density  $\rho_{\text{Halo}}$  and scale length  $l_s$ ). Histograms (diagonal) show marginalized distributions with the 16th, 50th, and 84th percentiles. Contours display covariances. Best-fit values with  $1\sigma$  uncertainties are reported in the legend. In the NFW case, maximum a posteriori (MAP) values deviate from the medians, highlighting weaker convergence compared to the ISO model in the main text.

## Appendix D: Unbound Scenarios

### D.1. Unbound solutions

Representative unbound or disfavored configurations. Panel i) Scenario I-b: eM1+sB+sA, ii) Scenario III-b: M1B+sB+sA, iii) Scenario IV-b: M1A+sA+sB, iv) Scenario III-a: M1B+sB, and v) Scenario V-b: progenitor destroyed; these could not satisfy the binding or tidal feasibility criteria. These fail because the total orbital energy is positive ( $E > 0$ ) or because the radius of the tidal in the pericenter exceeds the radius of the half-light of the progenitor, making the stripping of the tidal inefficient. Such cases help illustrate the explored parameter space, but are excluded from the main analysis. Orbits are shown in Fig. D.1.

Table A.1: Stream Points sA (7 points) and sB (13 points). These are observational inputs for the MCMC-EMCEE analysis (Foreman-Mackey et al. 2012). Satellite positions are also included. Spatial uncertainties are set by the projected angular scale and median seeing of  $0.8''$  (Galaz et al. 2015), corresponding to  $\pm 1$  kpc. Radial distance errors are propagated.

Object	$\alpha$ (2000)	$\delta$ (2000)	$x$ [kpc]	$y$ [kpc]	$r$ [kpc]
Malin 1	12:36:59.36	14:19:49.4	$0 \pm 1$	$0 \pm 1$	0
sA1: M1B	12:36:58.89	14:19:43.9	$12 \pm 1$	$-8 \pm 1$	$14 \pm 1$
sA2	12:36:58.42	14:19:39.4	$21 \pm 1$	$-13 \pm 1$	$25 \pm 1$
sA3	12:36:58.03	14:19:36.1	$30 \pm 1$	$-18 \pm 1$	$35 \pm 1$
sA4: M1A	12:36:57.62	14:19:32.9	$38 \pm 1$	$-24 \pm 1$	$45 \pm 1$
sA5	12:36:57.12	14:19:28.2	$47 \pm 1$	$-29 \pm 1$	$56 \pm 1$
sA6	12:36:56.78	14:19:26.8	$63 \pm 1$	$-38 \pm 1$	$74 \pm 1$
sA7	12:36:56.47	14:19:24.9	$77 \pm 1$	$-44 \pm 1$	$89 \pm 1$
sB1	12:36:59.98	14:20:07.1	$-11 \pm 1$	$29 \pm 1$	$31 \pm 1$
sB2	12:37:00.02	14:20:12.1	$-13 \pm 1$	$34 \pm 1$	$37 \pm 1$
sB3: M1C	12:37:00.36	14:20:16.8	$-22 \pm 1$	$42 \pm 1$	$47 \pm 1$
sB4	12:37:00.65	14:20:22.6	$-27 \pm 1$	$50 \pm 1$	$57 \pm 1$
sB5	12:37:01.03	14:20:27.6	$-34 \pm 1$	$59 \pm 1$	$69 \pm 1$
sB6	12:37:01.34	14:20:34.4	$-45 \pm 1$	$72 \pm 1$	$85 \pm 1$
sB7	12:37:01.68	14:20:41.3	$-52 \pm 1$	$80 \pm 1$	$95 \pm 1$
sB8	12:37:01.70	14:20:41.6	$-55 \pm 1$	$85 \pm 1$	$102 \pm 1$
sB9	12:37:02.69	14:20:56.4	$-69 \pm 1$	$105 \pm 1$	$125 \pm 1$
sB10	12:37:03.22	14:21:02.9	$-81 \pm 1$	$118 \pm 1$	$144 \pm 1$
sB11	12:37:03.55	14:21:12.2	$-92 \pm 1$	$131 \pm 1$	$160 \pm 1$
sB12	12:37:04.10	14:21:24.8	$-103 \pm 1$	$147 \pm 1$	$180 \pm 1$
sB13	12:37:04.85	14:21:37.8	$-119 \pm 1$	$167 \pm 1$	$205 \pm 1$
eM1	12:37:08.92	14:22:53.3	$-211 \pm 1$	$278 \pm 1$	$349 \pm 1$

Table B.1: Orbital scenarios detailing the best fitted **parameter ranges** and their underlying **physical motivation**. Refer to Table 6 for the complete tabulated best-fit parameters and Table B.2 to see the  $R_{Peri}$ ,  $R_{Apo}$ ,  $\epsilon$  best-fit parameter ranges.

Scenario	$z$ [kpc]	$V_{lg}$ [km s $^{-1}$ ]	PA [deg]	Justification
I-a-Radial: eM1+sB	$-294.43^{+172.90}_{-302.12}$	$250.27^{+162.21}_{-130.54}$	$40.00^{+1.48}_{-0.30}$	The satellite is projected near the NE part of the disc. We limited PA to quadrant I based on the stream's radial direction, and assumed negative $z$ (below the disc).
I-a-Polar: eM1+sB	$1.72^{+28.85}_{-30.18}$	$112.79^{+221.07}_{-88.64}$	$41.00^{+8.25}_{-1.41}$	A polar orbit, with the stream a projection of a circular orbit. We used positive $z$ . Orientation and morphology suggest infall from below; positive $z$ excluded.
II-b: M1C+sA+sB	$0.10^{+2.77}_{-2.52}$	$384.82^{+7.21}_{-10.21}$	$37.00^{+0.56}_{-0.54}$	Highly unconstrained test case with a distant satellite; wide ranges used to explore possible solutions.
III-a: M1B+sB	$-0.32^{+9.02}_{-7.80}$	$781.48^{+77.08}_{-73.86}$	$27.00^{+4.03}_{-3.97}$	Orbit near disc plane on southern side; PA range reflects motion direction.
IV-a: M1A+sA	$10.85^{+13.17}_{-13.96}$	$371.88^{+86.88}_{-89.19}$	$240.00^{+2.61}_{-2.66}$	Strong stream features suggest a decaying retrograde orbit entering from behind the disc.
V-a: sA	$-0.15^{+7.12}_{-6.87}$	$648.41^{+171.08}_{-176.05}$	$-240.00^{+1.56}_{-1.51}$	Stream curvature favors a transverse orbit westward; both $z$ signs allowed.
V-b: sB	$-0.19^{+6.93}_{-6.68}$	$703.99^{+133.72}_{-138.87}$	$37.00^{+0.82}_{-0.86}$	Wide $z$ range tests vertical impact trajectory; PA constrained by stream bending.

Table B.2: The table presents the final best-fit orbital geometry parameters—**pericenter** ( $R_{\text{peri}}$ ), **apocenter** ( $R_{\text{apo}}$ ), and **eccentricity** ( $\epsilon$ )—for each scenario. These results correspond to the two dark matter profiles explored: **ISO** and **NFW**. Refer to Table 6 for the complete tabulated set of final best-fit parameters and Table B.1 to see the  $z$ ,  $v_{\text{lg}}$ ,  $PA$  best-fit parameter ranges.

Scenario	$R_{\text{peri}}$ [kpc]	$R_{\text{apo}}$ [kpc]	$\epsilon$	Comments
I-a-Radial: eM1+sB	$182.05^{+238.77}_{-72.17}$	$1736.05^{+1681.03}_{-1137.98}$	$0.37^{+0.19}_{-0.10}$	High <b>eccentricity</b> ( $\epsilon \approx 0.37$ ) and large $R_{\text{apo}} \approx 1.7$ Mpc, indicating a loosely bound, highly elongated orbit.
I-a-Polar: eM1+sB	$159.90^{+41.98}_{-17.44}$	$416.76^{+1841.46}_{-63.05}$	$0.11^{+0.34}_{-0.02}$	Nearly <b>circular</b> ( $\epsilon \approx 0.11$ ) with the closest $R_{\text{peri}} \approx 160$ kpc. Apocenter uncertainty is the highest.
II-b: M1C+sA+sB	$199.36^{+2.51}_{-2.73}$	$1434.19^{+28.70}_{-40.84}$	$0.35^{+0.01}_{-0.01}$	Highly <b>elliptical</b> ( $\epsilon \approx 0.35$ ) with $R_{\text{apo}} \approx 1.4$ Mpc. Low uncertainty on $\epsilon$ suggests a robustly elongated shape.
III-a: M1B+sB	$215.44^{+17.32}_{-13.64}$	$682.37^{+50.86}_{-40.34}$	$0.14^{+0.03}_{-0.02}$	Compact, nearly <b>circular</b> ( $\epsilon \approx 0.14$ ) orbit with moderate $R_{\text{apo}} \approx 682$ kpc, suggesting a tightly bound satellite.
IV-a: M1A+sA	$202.08^{+13.04}_{-12.49}$	$565.20^{+59.18}_{-60.28}$	$0.12^{+0.02}_{-0.02}$	The most compact orbit overall, with the smallest $R_{\text{apo}} \approx 565$ kpc and very <b>low eccentricity</b> ( $\epsilon \approx 0.12$ ).
V-a: sA	$211.30^{+7.20}_{-7.67}$	$871.29^{+286.35}_{-226.89}$	$0.21^{+0.07}_{-0.07}$	Moderately <b>eccentric</b> ( $\epsilon \approx 0.21$ ). $R_{\text{peri}}$ is well-constrained, but $R_{\text{apo}}$ shows large uncertainties.
V-b: sB	$207.23^{+3.69}_{-3.60}$	$944.86^{+223.98}_{-225.36}$	$0.23^{+0.05}_{-0.07}$	Moderately <b>eccentric</b> ( $\epsilon \approx 0.23$ ) orbit. $R_{\text{peri}}$ is one of the most precisely determined values in the table.

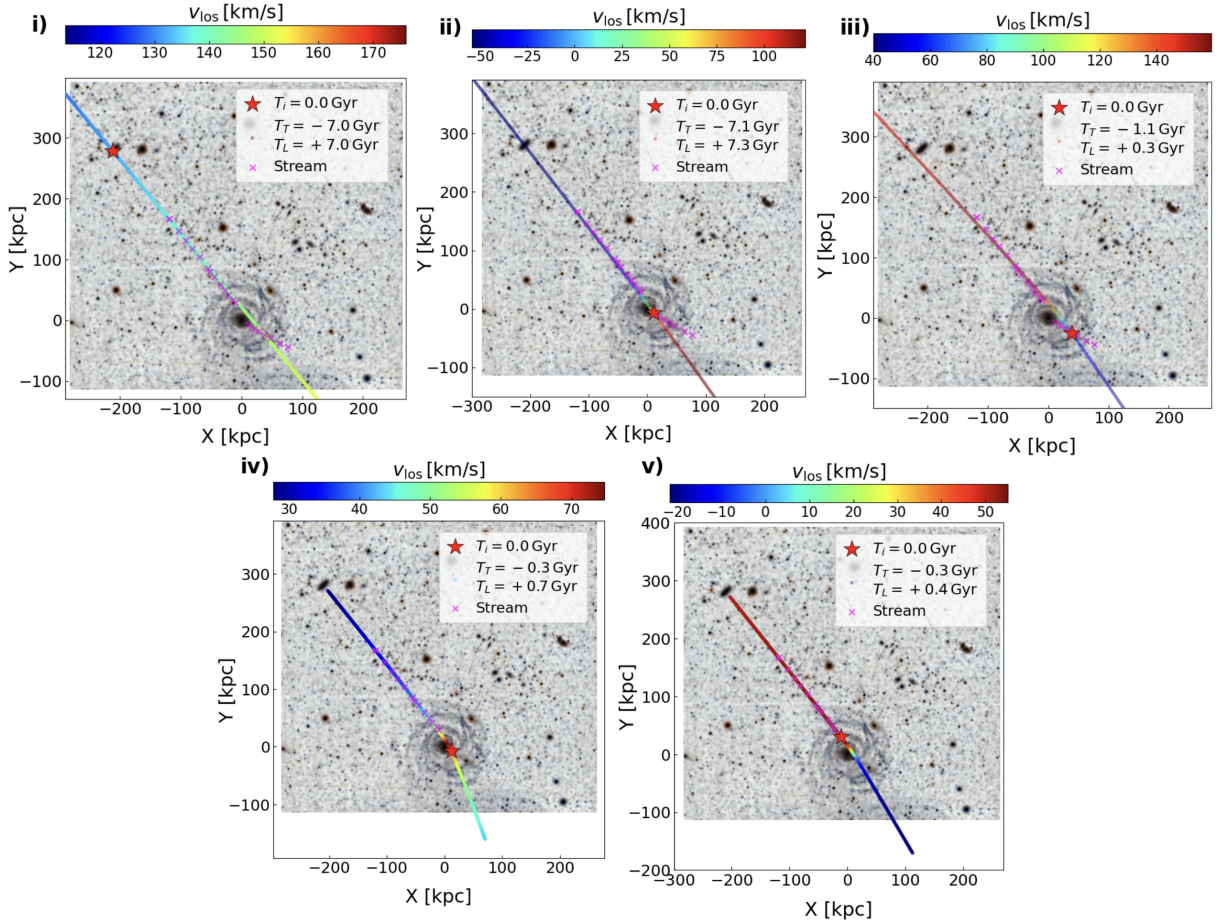


Fig. D.1: Examples of unbound or disfavored configurations. Panel i) Scenario I-b: eM1+sA+sB, ii) Scenario III-b: M1B+sA+sB, iii) Scenario IV-b: M1A+sA+sB, iv) Scenario III-a: M1B+sB, and v) Scenario V-b: progenitor destroyed; these fail to satisfy binding or tidal feasibility criteria.